Chapter 2
Heterogeneity in the Lithosphere

Geologists and geophysicists have numerous ways to investigate and characterize heterogeneity in the earth. Geophysical characterization includes measurement of physical properties such as seismic velocities and density of rocks. Geological characterization includes mineralogical composition and grain size distribution that are both controlled by the processes by which the rock evolved. Geologists observe the surface of the earth and analyze rocks that originated from within the earth for signs of heterogeneity. The wide variation of rocks erupted from volcanoes provides geochemical and geological evidence of heterogeneity within the earth. Tectonic processes such as folding, faulting, and large scale crustal movements associated with plate tectonics contribute to making the lithosphere heterogeneous. Rocks recovered from boreholes show wide variation and rapid changes in chemical composition with depth. Geophysical measurements in wells show correlation and lack of correlation with chemical composition of the rocks, indicating that mineral composition alone is not the only factor that controls the physical properties of rocks. Deterministic seismic studies reveal a wide spatial variation in elastic properties within the earth's lithosphere. Scattering of high-frequency seismic waves reveals the existence of small scale heterogeneities in the lithosphere.

In this chapter, we will give an overview of various types of observations to show and methods to evaluate the heterogeneous structure of the earth's lithosphere. We will also introduce basic mathematical methods to characterize the random fluctuation of medium properties.

2.1 Geological Evidence

The earth's crust contains a wide variation of rock types. Table 2.1 lists the P-wave velocity α and S-wave velocity β of some common rocks that compose the earth's crust. Seismic velocities are different for different rock types. The earth has heterogeneities on many scales. Rocks have crystals that range in size from

H. Sato et al., *Seismic Wave Propagation and Scattering in the Heterogeneous Earth: Second Edition*, DOI 10.1007/978-3-642-23029-5_2,

Table 2.1 Velocities of rocks in the earth's crust. (Data for near-surface rocks from Press 1966)

Rock type	Location	P-wave Vel. α	S-Wave Vel. β
Granite	Westerly, Rhode Is., U.S.A.	5.76 km/s	3.23 km/s
Quartz Monzonite	Westerly, Rhode Is., U.S.A.	5.26	2.89
Andesite	Colorado, U.S.A.	5.23	2.73
Basalt	Germany	5.0–6.4	2.7–3.2
Limestone	Argillaceous, Texas, U.S.A	5.71–6.03	3.04–3.04
Slate	Everett, Mass., U.S.A.	4.27	2.86

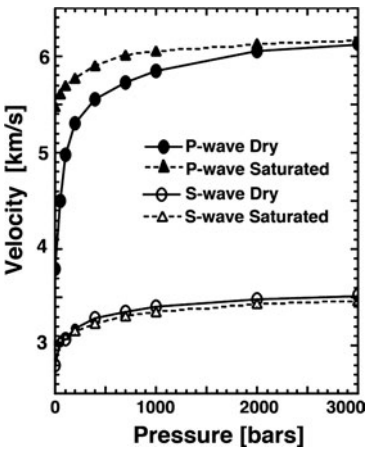

Fig. 2.1 Laboratory measurements of the variation of wave velocity in dry and water saturated Westerly granite. (Data from Nur and Simmons 1969, copyright by Elsevier)

fractions of mm to a few cm in scale. Properties of minerals that make up rocks in the earth's crust vary a great deal (Simmons and Wang 1971). For example, the bulk modulus of quartz, one of the major constituents of crustal rocks, is about 0.39×10^{12} dyn/cm^2 whereas that of the mineral plagioclase, another major constituent, is about 0.65×10^{12} dyn/cm^2 (Simmons and Wang 1971). Thus, the relative abundance of these two minerals in a rock can greatly influence its elastic properties.

In addition to mineralogy, fractures influence the elastic properties of a rock (Simmons and Nur 1968). Fractures range in size from submicroscopic to many tens of meters. Since fractures are more compliant than intact minerals, the spatial variations in fracture content and size can have a larger influence on elastic properties of crustal rocks than mineral composition. Figure 2.1 shows laboratory measurements of velocity variation with pressure for granite from Westerly, Rhode Island, U.S.A. The variation with pressure is due to the closure of fractures having lengths ranging from 0.01 mm to 1 cm and is typical of most crustal rocks. The P-wave velocity is more sensitive to the presence of fluids in the fractures than the S-wave velocity since fluids transmit compressional waves but not shear waves.

Anisotropy of rock properties can be significant and may vary with location, which increases rock heterogeneity. The presence of fractures can lead to anisotropy

of the elastic properties of the bulk rock. Fractures may have a preferential alignment that results from the way they were formed or due to the variation in stress magnitude as a function of orientation that causes some cracks to be open and some to be closed. Another type of anisotropy is a result of a layering of rocks, such as is present in many sedimentary formations. Tectonic processes may rotate the layering so that the preferential orientation of fast and slow directions of anisotropic media are not aligned with horizontal and vertical directions. A general overview of anisotropy can be found in Helbig and Thomsen (2005) and Tsvankin et al. (2010).

Intrusions of magma into preexisting country rock can result in dikes and sills that have different composition from the country rock. These dikes and sills can be as small as a few mm wide resulting in a rapid spatial variation in rock properties. Variations in rock properties in volcanic regions can occur on scales of a few m to a few km due to variations in composition of magmas erupted at differing stages of a volcano's life. The variation in tectonic provinces occurs over tens to hundreds of km. For example, the Cascade range in the western U.S.A. is largely made up of young volcanic rocks whose elastic properties are dramatically different from those of the old Precambrian rocks of the central U.S.A.

The earth's crust has largely been formed through magmatic processes. Large silicic batholiths like the Sierra Nevada, U.S.A. are the intrusive remains of volcanic complexes that have been eroded away. Geochemists argue that silicic rocks that intrude into the shallow crust and erupt at volcanoes were formed by either fractionation of iron-rich rocks that intrude into the lower crust from the mantle or by the transfer of heat from intruded iron-rich mantle rocks to silicic rocks in the deep crust (Perry et al. 1990). In either case, there will be high-velocity material remaining within the silicic crust. The velocity of the high-density material may be as high as 7.5 km/s (Fountain and Christensen 1989). If heat is transferred from mantle-derived magmas, the resulting magmas may have velocities of about 7.0 km/s. The intrusion process thus results in considerable heterogeneity in the earth's crust.

Characterization of heterogeneity in sedimentary rocks receives considerable attention because these rocks contain a majority of the world's hydrocarbons. Heterogeneity in sedimentary formations has many causes including changes in the source rocks from which the sediments were formed, variations in the cementing rocks together, variations in porosity and pore fluids, and the tectonic processes that act on the rocks after deposition. The deterministic heterogeneity in many sedimentary rocks is well characterized by the extensive amount of seismic imaging of various types, borehole logging, and geological characterization that has been conducted during the exploration for and development of hydrocarbon resources.

Other geological processes that contribute to heterogeneity in the lithosphere include erosion and metamorphism that act to transport rocks or change their character in place. Tectonic processes, such as faulting and folding, move rocks relative to one another and result in heterogeneity. Large scale movements of lithospheric plates distribute rocks having a common origin over a wide range. The collision of tectonic plates at plate boundaries, such as subduction zones or collision zones, causes rocks of differing types to come into contact.

2.2 Birch's Law

There are good correlation among P and S-wave velocities and mass density. From experimental data on rocks of many types, Birch (1960, 1961) found that seismic velocity increases roughly linearly with mass density for rocks having the same mean atomic weight, which is the atomic weight of the minerals that comprise the rocks averaged in proportion to the mass they contribute to the rock. Mean atomic weight for most crustal rocks ranges from about 21 for silica-rich rocks like granite to 22 for iron-rich igneous rocks. Figures 2.2a and b show P- and S-wave velocities in km/s measured at 10 kbar (1 GPa) pressure on common lithospheric rocks having mean atomic weights between 20.5 and 22.5 plotted against mass density in g/cm^3, respectively, where straight lines are linear regression lines. For P-waves measured at 10 kbar pressure, Birch (1961) found $\alpha = 3.05\rho - 1.87$ for rocks having mean atomic weight ~21. The relationships among velocity and mass density is called Birch's law. Kanamori and Mizutani (1965) found $\alpha = 2.8\,\rho - 1.3$ at 6 kbar (0.6 GPa) for dunite, peridotite and eclogite in Japan. Christensen (1968) made laboratory measurements on rocks typical of those suspected to compose the upper mantle and found that S-wave velocity varies as $\beta = 1.63\ \rho - 0.88$ at 10 kbar for mean atomic weight ~22. Manghnani et al. (1974) measured both P- and S-wave velocities for granulite facies rocks and eclogite and found $\alpha = 2.87\rho - 1.85$ and $\beta = 1.40\rho - 0.33$ at 10 kbar where mean atomic weight ~22.

Christensen and Mooney (1995) reported on laboratory P-wave velocity measurements of many rocks that compose the earth's crust. They grouped the rocks into a total of 29 categories by common rock type. They made measurements using a common laboratory technique on all the rocks at various pressures corresponding

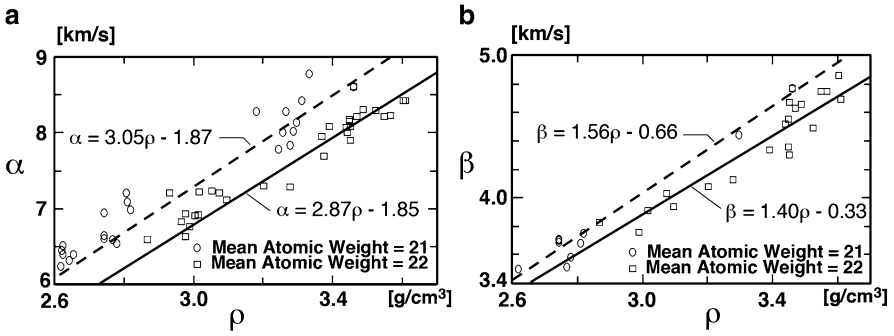

Fig. 2.2 (**a**) P-wave velocity against mass density and (**b**) S-wave velocity against mass density for common lithospheric igneous and metamorphic rocks measured at 10 kbar (1 GPa). Dashed lines show fits to data for rocks having mean atomic weights between 20.5 and 21.5 by Birch (1961) for P-waves and Manghnani et al. (1974) for S-waves. Solid lines show fits for rocks having mean atomic weights between 21.5 and 22.5 by Manghnani et al. (1974) for both P- and S-waves. Data from Manghnani et al. (1974) and Birch (1960, 1961)

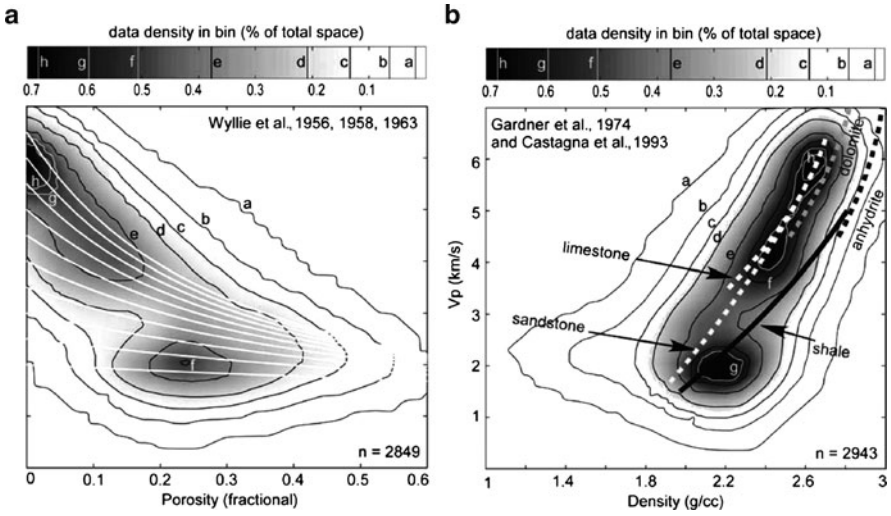

Fig. 2.3 (**a**) P-wave velocity against porosity and (**b**) P-wave velocity against mass density for sedimentary rocks. (Kenter et al. 2007, copyright by the Society of Exploration Geophysics)

to depths of 5 to 50 km. At a depth of 20 km, they reported $\alpha = 2.41\rho - 0.454$ for all rocks except volcanic rocks and monomineralic rocks. For typical rocks in the crust and upper mantle which is predominantly peridotite, Christensen and Mooney (1995) proposed that a better fit to the data is obtained using a relationship of the form $\alpha^{-1} = -2.3691 \cdot 10^{-3}\rho^3 + 0.2110$.

Kenter et al. (2007) summarized the relation between P-wave velocity and density of sedimentary rocks as shown in Fig. 2.3b. Regression lines are shown by a broken gray line for sandstone and a black solid line for shale. Their velocity gradients against mass density for sedimentary rocks are much larger than those for silica-rich rocks like granite and iron-rich igneous rocks. They reported that the wave velocity is strongly controlled by porosity as shown in Fig. 2.3a.

Christensen (1996) reported on laboratory measurements of P- and S-wave velocities of 678 crustal rocks. He investigated the average ratio of P- to S-wave velocity α_0/β_0 for crustal rocks by comparing his data with average crustal composition obtained from seismic refraction studies of the crust that are summarized by Christensen and Mooney (1995). He found the velocity ratio $\alpha_0/\beta_0 = 1.768$ for the continental crust. He estimates that Poisson's ratio varies from 0.253 in the upper crust to 0.283 at a depth of 30 km and down to 0.279 in the lower crust. We note that Poisson's ratio of some sedimentary rocks has been found to be greater than 0.4 (Kenter et al. 2007).

2.3 Random Inhomogeneity

2.3.1 Velocity Inhomogeneity Revealed from Well-Logs

Direct evidence for the existence of random inhomogeneities can be found in log data from wells. Figure 2.4a shows wave velocity and density log data from well YT2 drilled through lava, tuff, and volcanic breccia in Kyushu, Japan. The velocity structure was determined from the travel times of ultrasonic waves having frequencies of a few tens of kHz. Rock mass density is measured from the intensity of gamma rays received at a borehole detector. The intensity of received gamma rays can be shown to be a function of the formation density (Telford et al. 1976).

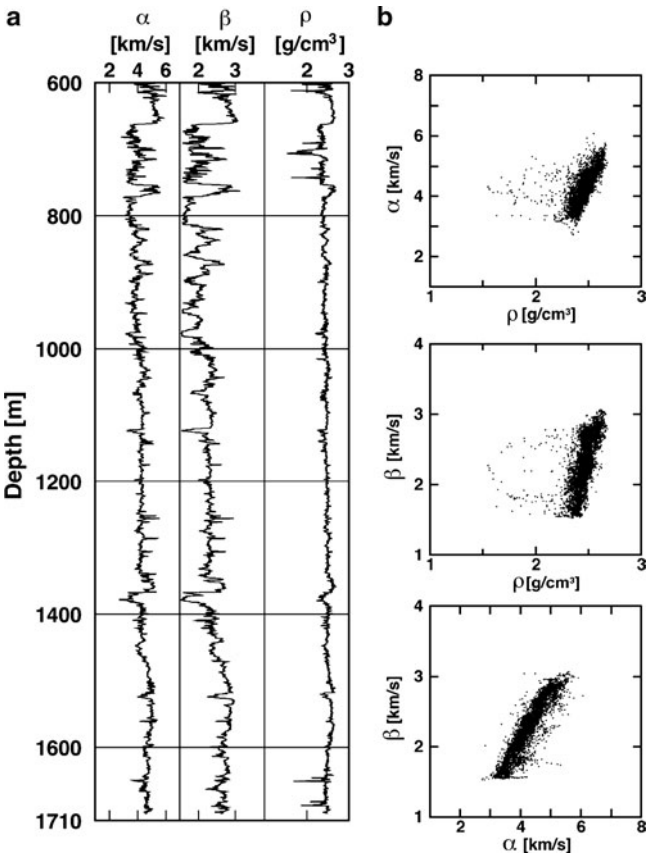

Fig. 2.4 (**a**) Well-logs showing P- and S-wave velocities and mass density vs. depth for well YT2 in Kyushu, Japan. (**b**) Scattergrams showing correlation among the physical properties measured at the same depth. (Shiomi et al. 1997, copyright by Willey)

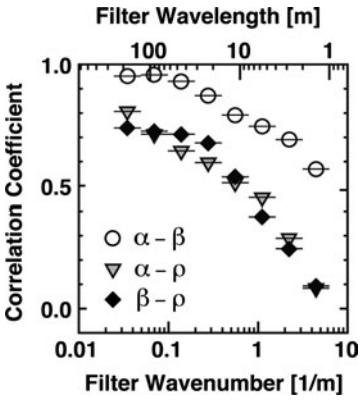

Fig. 2.5 Correlation coefficients between different physical properties calculated from bandpass-filtered traces of the logs of well YT2 in Kyushu, Japan shown in Fig. 2.4a. (Shiomi et al. 1997, copyright by Willey)

Wave propagation velocity usually increases with increasing depth in the earth; however, considerable spatial variation of velocity is evident in the logs. As shown in the scattergram for a selected depth range in Fig. 2.4b, we find that the P-wave velocity has a clear correlation with S-wave velocity and each wave velocity has a positive correlation with mass density. Regression lines of scattergrams in Fig. 2.4b are roughly approximated as $\alpha \approx 7\rho - 13$ and $\beta \approx 6\rho - 12.5$, where velocity is in km/s and density is in g/cm^3.

Making a scattergram from bandpass-filtered well-log measurements of different parameters at the same depth, we can estimate the correlation coefficient. The correlation coefficient generally decreases as the pass band center-wavelength becomes shorter. The correlation coefficient between P- and S-wave velocities is as large as 0.7 even when the center-wavelength is as small as a few meters as shown in Fig. 2.5. Correlation coefficients of the P- and S-wave velocities with mass density drop to less than 0.7 for center-wavelengths less than 30 m. We note that the transducer-receiver separation for the velocity logging tool of 0.6 m works as a high-wavenumber-cut filter.

2.3.2 Mathematical Description of Random Media

Spectral characteristics of inhomogeneities, such as those found in well-log data and elsewhere in the earth, are conveniently described by using a statistical model, where we imagine an "ensemble" of random media that have the same statistical characteristics such as common autocorrelation function (ACF) or common power spectral density function (PSDF). Synthesizing waves in many realizations of random media, we take the average of different kinds of physical quantities constructed from various moments of wavefields over the given ensemble for comparison with observed quantities.

2.3.2.1 Ensemble of Homogeneous and Isotropic Random Media

We suppose that wave velocity V is not a constant but a sum of the mean velocity V_0 and the perturbed velocity δV which depends on the location $\mathbf{x}$ as

$$V(\mathbf{x}) = V_0 + \delta V(\mathbf{x}) = V_0 [1 + \xi(\mathbf{x})], \tag{2.1}$$

where non-dimensional quantity $\xi(\mathbf{x}) \equiv \delta V(\mathbf{x}) / V_0$ is the fractional fluctuation of wave velocity. We study the case that $\xi(\mathbf{x})$ is a random function of coordinate $\mathbf{x}$. We imagine an ensemble of random media $\{\xi\}$, and denote the average over the ensemble by angular brackets $\langle \ldots \rangle$, where the mean velocity is chosen so that $V_0 = \langle V(\mathbf{x}) \rangle$ and $\langle \xi(\mathbf{x}) \rangle = 0$.

ACF and PSDF for Stationary Process

When the randomness is stationary (homogeneous) over all space, the ensemble average of a product $\xi(\mathbf{y})\,\xi(\mathbf{y}+\mathbf{x})$ is independent of coordinate $\mathbf{y}$ but a function of lag $\mathbf{x}$ only. To characterize the random media, we define the ACF of the fractional velocity fluctuation as

$$R(\mathbf{x}) \equiv \langle \xi(\mathbf{y})\,\xi(\mathbf{y}+\mathbf{x}) \rangle, \tag{2.2}$$

which gives a statistical measure of the spatial scale and the magnitude of medium inhomogeneity. Furthermore, we often require isotropy of randomness, then ACF becomes a function of the lag distance $r \equiv |\mathbf{x}|$ only. The magnitude of the fractional fluctuation is given by the mean square (MS) fractional fluctuation $\varepsilon^2 \equiv R(0)$. The spatial variation of randomness is well characterized by correlation distance a as $R \ll \varepsilon^2$ for $r \gg a$. The correlation distance a is often defined to satisfy $R(a) = \varepsilon^2/e$.

The Fourier transform of the ACF gives the PSDF as

$$P(\mathbf{m}) = P(m) = \widetilde{R}(\mathbf{x}) = \iiint_{-\infty}^{\infty} R(\mathbf{x})\, e^{-i\mathbf{m}\mathbf{x}} d\mathbf{x},$$
$$R(\mathbf{x}) = R(r) = \frac{1}{(2\pi)^3} \iiint_{-\infty}^{\infty} P(\mathbf{m})\, e^{i\mathbf{m}\mathbf{x}} d\mathbf{m}, \tag{2.3}$$

where $\mathbf{m}$ is the wavenumber vector and $m = |\mathbf{m}|$. A tilde means the Fourier transform in space. Performing the integral over solid angle in spherical coordinates, we have

$$R(r) = \frac{1}{2\pi^2 r} \int_0^{\infty} \sin rm\; P(m)\, m\, dm. \tag{2.4}$$

In order to let the above integral be finite, the PSDF must satisfy $P(m) \to m^{\nu}$ as $m \to 0$, where $\nu > -3$ since $\sin mr/mr \approx 1$.

Structure Function for Process of Stationary Increments

When random function $\xi(\mathbf{x})$ is not strictly stationary (homogeneous) over all space but locally stationary (homogeneous), the ensemble average of difference $\xi(\mathbf{y}+\mathbf{x}) - \xi(\mathbf{y})$ is independent of coordinate $\mathbf{y}$ but a function of lag $\mathbf{x}$ only. Furthermore, when the structure function

$$D(\mathbf{x}) \equiv \left\langle [\xi(\mathbf{y}+\mathbf{x}) - \xi(\mathbf{y})]^2 \right\rangle \tag{2.5}$$

is a function of lag $\mathbf{x}$ only, the random process is called a process of stationary increments. The structure function $D(\mathbf{x})$ is invariant even if we add some constant to the fractional fluctuation ξ. The stationary process is considered a special case of a process of stationary increments. In this case, there is a one-to-one correspondence:

$$D(\mathbf{x}) = 2R(0) - 2R(\mathbf{x}). \tag{2.6}$$

The finiteness of the structure function loosen the restriction as $\nu > -5$ for $P(m) \to m^{\nu}$ as $m \to 0$.

Realizations of Random Media

For the numerical study of wave propagation, it is necessary to make realizations of random media for a given PSDF $P(\mathbf{m})$. Using $\tilde{\xi}(\mathbf{m}) = \sqrt{P(\mathbf{m})}$ as the amplitude spectrum, we can synthesize a random medium sample $\xi(\mathbf{x})$ in space by using the Fourier transform as

$$\xi(\mathbf{x}) = \frac{1}{(2\pi)^3} \iiint_{-\infty}^{\infty} \sqrt{P(\mathbf{m})} e^{i\phi(\mathbf{m})} e^{i\mathbf{m}\mathbf{x}} d\mathbf{m}, \tag{2.7}$$

where the phase spectrum $\phi(\mathbf{m})$ is chosen to be random between 0 and 2π. Changing different seeds for the generation of random phase spectra, we are able to synthesize different realizations of random media as shown in Fig. 2.6. Those examples schematically illustrate different types of 2-D random media for the same ε and a.

2.3.2.2 Various Types of ACF and PSDF

There are several types of ACFs of random media that are convenient to use for the study of wave propagation (e.g. Ishimaru 1978; Klimeš 2002). In the following,

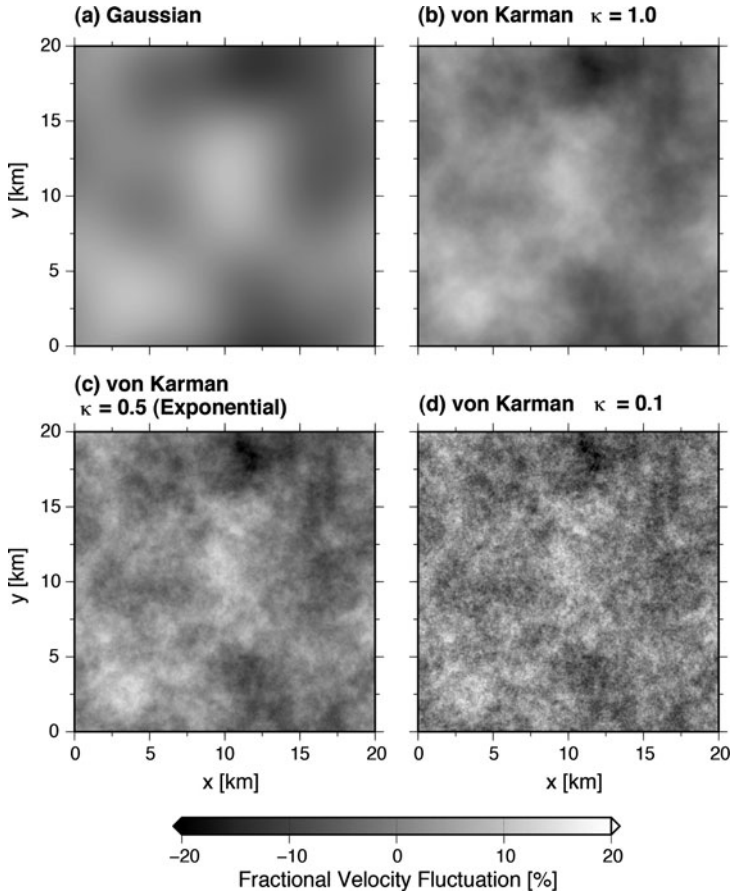

Fig. 2.6 Density plots of 2-D random medium samples, where $a = 5\,\mathrm{km}$ and $\varepsilon = 0.05$: (**a**) Gaussian ACF. (**b**) – (**d**) von Kármán type ACFs with different κ-values

we introduce several types of mathematically tractable ACFs and their PSDFs for random media which are homogeneous and isotropic.

Gaussian ACF

The most tractable ACF is a Gaussian ACF (see Fig. 2.7a) as given by

$$R(\mathbf{x}) = R(r) = \varepsilon^2 e^{-r^2/a^2}. \tag{2.8}$$

The PSDF is also Gaussian. For the 3-D case, the PSDF is

$$P(\mathbf{m}) = P(m) = \varepsilon^2 \sqrt{\pi^3} a^3 e^{-m^2 a^2/4}. \tag{2.9}$$

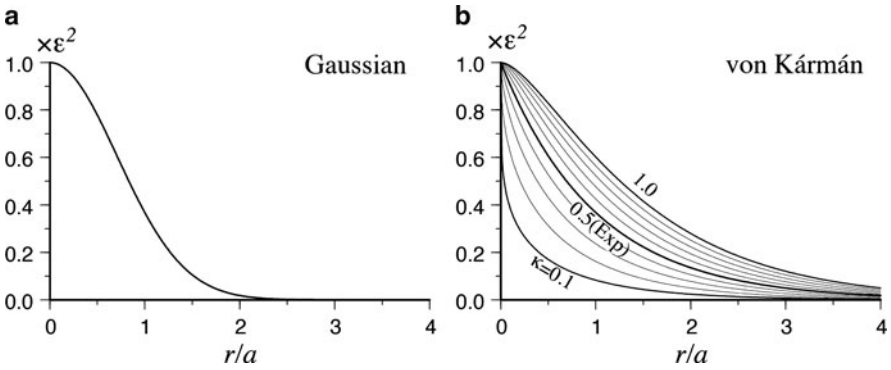

Fig. 2.7 Plots of (**a**) Gaussian ACF and (**b**) von Kármán ACF in 3-D, where a curve for $\kappa = 0.5$ is an exponential ACF

The Gaussian ACF is used to describe media that are poor in short wavelength components since the PSDF goes rapidly to zero for large m. Many theoretical models are developed by assuming a Gaussian ACF because of its mathematical tractability.

Exponential ACF

The next example is an exponential ACF (see a bold line in Fig. 2.7b):

$$R(\mathbf{x}) = R(r) = \varepsilon^2 e^{-r/a}. \tag{2.10}$$

For the 3-D case, the PSDF is

$$\begin{aligned} P(\mathbf{m}) = P(m) &= \frac{8\pi\varepsilon^2 a^3}{\left(1 + a^2 m^2\right)^2} \\ &\propto (am)^{-4} \quad \text{for} \quad am \gg 1. \end{aligned} \tag{2.11}$$

The PSDF obeys a power law for large wavenumbers as illustrated by a bold line in Fig. 2.8a.

von Kármán ACF

An extension of an exponential ACF, a von Kármán ACF (see Fig. 2.7b) is given by

$$R(\mathbf{x}) = R(r) = \frac{\varepsilon^2 2^{1-\kappa}}{\Gamma(\kappa)} \left(\frac{r}{a}\right)^{\kappa} K_{\kappa}\left(\frac{r}{a}\right) \quad \text{for} \quad \kappa = 0 \sim 1, \tag{2.12}$$

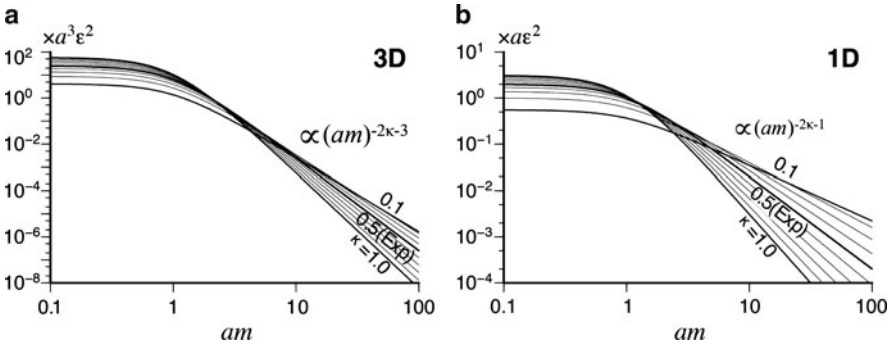

Fig. 2.8 PSDFs of von Kármán type random media for different κ values in (**a**) 3-D and (**b**) 1-D

where $\Gamma(\kappa)$ is the gamma function and K_κ is the modified Bessel function of the second kind of order κ. We note that $\lim_{z\to 0} z^\kappa K_\kappa(z) = 2^{-1+\kappa}\Gamma(\kappa)$ (Abramowitz and Stegun 1970, p. 375). For the 3-D case, the PSDF is

$$P(\mathbf{m}) = P(m) = \frac{8\pi^{3/2}\Gamma(\kappa+3/2)\varepsilon^2 a^3}{\Gamma(\kappa)(1+a^2m^2)^{\kappa+3/2}} \propto (am)^{-2\kappa-3} \quad \text{for} \quad am \gg 1. \tag{2.13a}$$

The PSDF obeys a power law for large wavenumbers ($am \gg 1$) as illustrated in Fig. 2.8a, where the power-low decay is controlled by parameter κ. A power-law decay for large wavenumbers means that the PSDF for von Kármán type random media is rich in short wavelength components compared with that of Gaussian type random media. The von Kármán ACF with $\kappa = 0.5$ coincides with the exponential ACF. We will see that a von Kármán type ACF is more appropriate for describing random velocity inhomogeneities of the real earth medium compared with a Gaussian type because of its power-law characteristic.

Replacing $r \to |x|$ in (2.12), we have a von Kármán type ACF for a 1-D space. The corresponding PSDF is

$$P_{1D}(m) = \frac{2\pi^{1/2}\Gamma(\kappa+1/2)\varepsilon^2 a}{\Gamma(\kappa)(1+a^2m^2)^{\kappa+1/2}}, \tag{2.13b}$$

where $m = |m_x|$ (see Fig. 2.8b). Replacing $r \to \sqrt{x^2+y^2}$ in (2.12), we have a von Kármán type ACF in a 2-D space and the corresponding PSDF as

$$P_{2D}(m) = \frac{4\pi\Gamma(\kappa+1)\varepsilon^2 a^2}{\Gamma(\kappa)(1+a^2m^2)^{\kappa+1}}, \tag{2.13c}$$

where $m = \sqrt{m_x^2+m_y^2}$. Comparing PSDFs at large wavenumbers for different dimensions, we see the power of wavenumber is $-2\kappa-$ (Euclidean dimension).

Proof of the Relation Between (2.12) and (2.13a)

Substituting (2.13a) into (2.3), we have

$$R(r) = \frac{1}{(2\pi)^3}\int_0^{2\pi} d\varphi_m \int_0^{\pi} \sin\theta_m e^{imr\cos\theta_m} d\theta_m \int_0^{\infty} \frac{8\pi^{3/2}\varepsilon^2 a^3 \Gamma(\kappa+3/2)}{\Gamma(\kappa)(1+a^2m^2)^{\kappa+3/2}} m^2 dm$$
$$= \frac{1}{(2\pi)^2}\int_0^{\infty} \frac{2\sin mr}{mr} \frac{8\pi^{3/2}\varepsilon^2 a^3 \Gamma(\kappa+3/2)}{\Gamma(\kappa)(1+a^2m^2)^{\kappa+3/2}} m^2 dm$$
$$= \frac{4\varepsilon^2 a^3 \Gamma(\kappa+3/2)}{\sqrt{\pi} r \Gamma(\kappa)} \int_0^{\infty} \frac{m\sin mr}{(1+a^2m^2)^{\kappa+3/2}} dm, \tag{2.14}$$

where (m, θ_m, φ_m) are spherical coordinates in wavenumber space. The integral in the last line can be evaluated by using the integration by parts:

$$\int_0^{\infty} \frac{m\sin mr}{(1+a^2m^2)^{\kappa+3/2}} dm = -\frac{\sin mr}{a^2(1+2\kappa)(1+a^2m^2)^{\kappa+1/2}}\Bigg|_0^{\infty}$$
$$+ \frac{r}{a^2(1+2\kappa)} \int_0^{\infty} \frac{\cos mr}{(1+a^2m^2)^{\kappa+1/2}} dm$$
$$= \frac{\sqrt{\pi} r^{\kappa+1}}{a^{\kappa+3} 2^{\kappa+1} (\kappa+1/2)\Gamma(\kappa+1/2)} K_{\kappa}\left(\frac{r}{a}\right)$$
$$= \frac{2^{1-\kappa}\sqrt{\pi}\, r}{4a^3\Gamma(\kappa+3/2)} \left(\frac{r}{a}\right)^{\kappa} K_{\kappa}\left(\frac{r}{a}\right), \tag{2.15}$$

where we used the integral representation of the modified Bessel function of the second kind (see Abramowitz and Stegun 1970, p. 376). Thus (2.12) is obtained.

Evaluation of PSDF in 1-D from that in 3-D

When 3-D random media are isotropic, we can evaluate the PSDF along a line by taking samples along the z-axis:

$$P_{1D}(m_z) \equiv \int_{-\infty}^{\infty} R(0,0,z)\, e^{-im_z z} dz$$
$$= \int_{-\infty}^{\infty} \left[\frac{1}{(2\pi)^3} \iiint_{-\infty}^{\infty} P(\mathbf{m}')\, e^{im'_z z} d\mathbf{m}'\right] e^{-im_z z} dz$$
$$= \frac{1}{(2\pi)^2} \iint_{-\infty}^{\infty} P\left(m'_x, m'_y, m_z\right) dm'_x dm'_y. \tag{2.16}$$

In the case of von Kármán type ACF, substituting (2.13a) into the above equation, we obtain the PSDF in 1-D (2.13b) as

$$P_{1D}(m_z) = \frac{1}{(2\pi)^2} \iint_{-\infty}^{\infty} \frac{8\pi^{3/2}\varepsilon^2 a^3 \Gamma(\kappa + 3/2)}{\Gamma(\kappa)\left[1 + a^2\left(m_x'^2 + m_y'^2 + m_z^2\right)\right]^{\kappa+3/2}} dm_x' dm_y'$$
$$= \frac{2\pi^{1/2}\Gamma(\kappa + 1/2)\,\varepsilon^2 a}{\Gamma(\kappa)\left(1 + a^2 m_z^2\right)^{\kappa+1/2}}. \tag{2.17}$$

This relation between different dimensions is a key for the interpretation of well logs, which are 1-D sample data.

Nonisotropic ACF

Unless otherwise noted, we assume that the randomness is isotropic in this book. Here we show one example of nonisotropic ACF. For sediments, we often see that the correlation distance in the vertical direction is shorter than that in the horizontal direction. A typical example is a nonisotropic Gaussian ACF:

$$R(\mathbf{x}) = \varepsilon^2 e^{-\frac{x^2}{a_x{}^2} - \frac{y^2}{a_y{}^2} - \frac{z^2}{a_z{}^2}}, \tag{2.18}$$

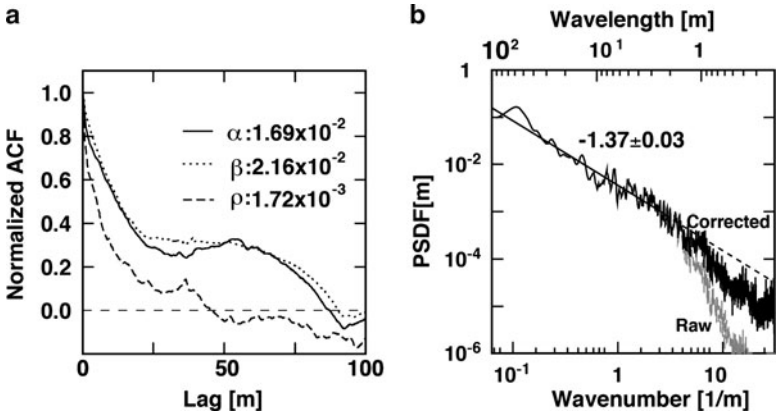

Fig. 2.9 Statistical characteristics of well-log data from well YT2 in Kyushu, Japan for a depth range of 600–1700 m (see Fig. 2.4a): (**a**) Normalized ACFs for fractional fluctuations of three physical properties, where numerals are the MS fractional fluctuation for each property. (**b**) PSDF of the P-wave velocity fractional fluctuation, where gray shows raw data and dark the data after logging tool correction, where numerals are the power index and its standard deviation. (Shiomi et al. 1997, copyright by Willey)

where a_x, a_y and a_z are correlation distances for the x-, y- and z-components, respectively.

2.3.3 *ACF of Velocity Inhomogeneity Revealed from Well-Logs and Rock Samples*

If we consider that well-log data is a stationary random process, we can calculate the ACF from the spatial average instead of the ensemble average. Figure 2.9a shows normalized ACFs $R(x)/R(0)$ of log data obtained from well YT2 for velocities and density (see Fig. 2.4a). Correlation distances scatter over a few tens of meters for these sampled data; however, the shape near the zero lag distance is not consistent with a Gaussian ACF but more closely follows exponential or von Kármán type ACFs. Figure 2.9b shows the PSDF of the P-wave velocity fractional fluctuation in well YT2. The PSDF decreases according to the -1.37 th power of wavenumber for a wide range of wavelengths from one meter to a hundred meters, where the high-wavenumber-cut filtering effect due to the logging tool has been corrected (Shiomi et al. 1997). A similar power-law characteristic was found for the KTB deep wells in Germany (Wu et al. 1994), where the power is reported to be -1.1. As the total length of log data increases, the power law has been found to hold well for an increased range of wavenumbers indicating self-affinity. Suzuki et al. (1981) reported that an exponential type ACF well fits the P-wave velocity fluctuations measured in logs of pretertiary basement rock in Kanto, Japan.

The ratio of the scale length in the horizontal direction to that in the vertical direction was estimated by analysis of log data from closely spaced wells at the KTB deep wells and found to be 1.8 (Wu et al. 1994). The difference in correlation length scales measured for borehole data may be due to the characteristic thickness of rock layers in the region under study. If the boreholes cross many rock layers in the study region, as was the case for the KTB deep wells, the characteristic length in the vertical direction may be smaller than in the horizontal direction. If no layers are encountered and the rock mass is geologically homogeneous, the elastic heterogeneity may be dominated by microfractures, which may be isotropically oriented, leading to similar ACFs in the vertical and horizontal directions.

Digitizing the lithological map of the Ivrea zone in northern Italy, which is considered a typical exposure of the lower continental crust, Holliger and Levander (1992) estimated the ACF in two orthogonal directions. They found that the ACF is a von Kármán type having nonisotropic randomness: the shorter correlation distance is $150 - 180$ m and the longer is $550 - 750$ m, and the aspect ratio is $3 - 5$.

There are reports on measurements of the ACF on the scale of a grain size. Granite is composed of feldspar, quartz, and biotite. Assigning the P-wave velocity of each mineral to appropriate locations on a surface photo image of a granite sample, Sivaji et al. (2002) and Fukushima et al. (2003) made 1-D velocity distributions. Then they calculated the ACF and PSDF of the fractional fluctuation

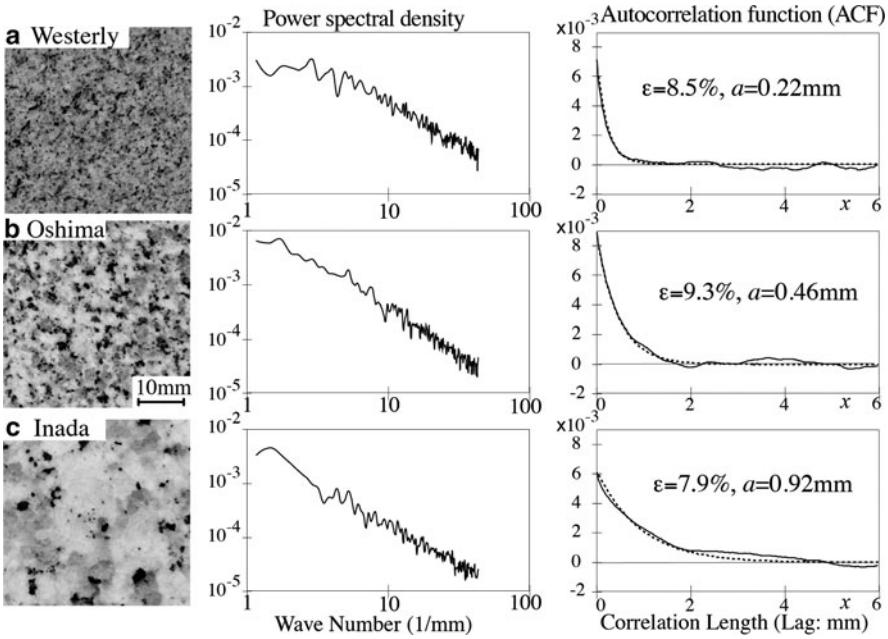

Fig. 2.10 Surface images (left), PSDF (middle) and ACF (right) of the fractional fluctuation of P-wave velocity for (**a**) Westerly, (**b**) Oshima, and (**c**) Inada granites. A dashed curve shown on the ACF indicates the best-fit exponential function. (Sivaji et al. 2002, copyright by Willey)

of P-wave velocity for granite samples as illustrated in Fig. 2.10. Though RMS fractional fluctuations are the same order, correlation distances representing roughness are different: 0.92, 0.46, and 0.22 mm for Inada, Oshima and Westerly granites, respectively. We note that each ACF is well approximated by an exponential function as shown by a dashed curve. Each PSDF is proportional to a power of wavenumber, which is approximated by a straight line in the log–log plot.

2.4 Deterministic Imaging Using Seismological Methods

One of the main focuses of seismology is the deterministic characterization of the spatial heterogeneity of the earth's lithosphere. These efforts are undertaken to better understand geological hazards like earthquakes and for economic as well as purely scientific goals. Characterizing the spatial heterogeneity of the lithosphere has enabled investigators to better understand the mechanism by which the earth's crust is formed, volcanic processes, and the nature of active seismic zones. In petroleum exploration, the shallow crust is investigated and subsurface structures that are considered to be good petroleum reservoirs are identified and characterized. For each study of subsurface structure, the spatial resolution of the desired

information about structure must be determined prior to data collection. A brief discussion of the role that various seismic techniques play in the determination of crustal structure can be found in Braile et al. (1995).

The reflection and refraction methods are widely used to characterize the crust. Refractions from the Moho provided the first direct evidence of the large contrast in seismic velocity between the crust and mantle. In current applications, arrival times and complete waveforms including amplitude and phase information are used in the reflection and refraction methods. Refraction studies are commonly used for studying regional seismic structure to depths as great as the Moho. Sizes of regions studied are generally on the order of a few tens to hundreds of km. Reflection studies are generally used on a more local scale for studies of a few to a few tens of km and to depths of up to 15 km although the extension of reflection methodologies have been done to study deep earth structure. Seismic tomography was introduced in the 1970s as an extension of the methods developed in materials testing and medical imaging. Initially seismic tomography was applied only to arrival times but more recent developments take account of waveform characteristics (e.g. Pratt 1999). Seismic tomography can be conducted on scales ranging from laboratory scale to the whole earth.

2.4.1 Refraction Surveys

The refraction technique is probably the oldest method used to characterize the earth's crust. Although refraction studies conducted today generally provide less resolution of crustal structure than reflection studies used for petroleum exploration, refraction studies do provide information about larger regions of the crust. As conducted today, refraction surveys can be considered transmission surveys or refraction combined with wide-angle reflection surveys since waves other than refractions are identified in the data collected and provide additional constraints on the derived models.

Processing methods for refraction seismic studies include forward modeling of travel times, forward modeling of waveforms using methods such as finite difference or reflectivity (Mooney 1989), and travel-time tomography (Zelt and Smith 1992). Each method has limitations: forward modeling of travel times may provide some information about crustal heterogeneity but provides little information about uniqueness of the derived model. Forward modeling of waveforms provides constraints from data of both amplitudes and phase and can result in more reliable models. Inversion of travel times provides information about uniqueness of the model and usually provides a good fit between predicted arrival times and measured times, but the limited angles at which rays propagate in refraction surveys limit the resolving power of this method.

Christensen and Mooney (1995) summarized results of refraction surveys made worldwide and discussed the implications of these surveys for our understanding of crustal composition. They divided the results into those obtained in five tectonic provinces and generated average P-wave velocity structural models as illustrated in

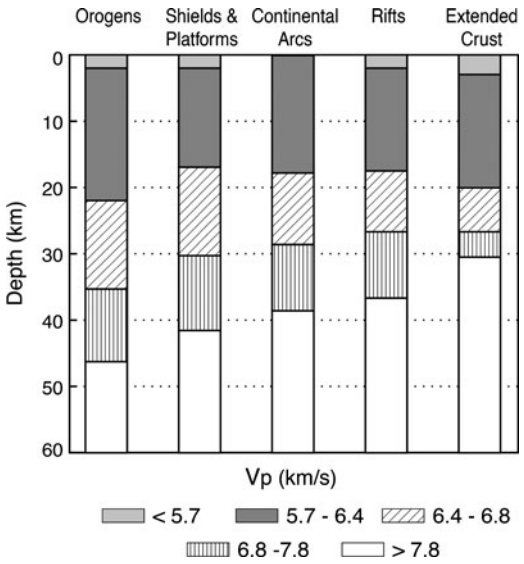

Fig. 2.11 Compilation of average layered P-wave velocity structures for five tectonic provinces based on results of measurements made worldwide. (Christensen and Mooney 1995, copyright by the American Geophysical Union)

Fig. 2.11. The layered velocity structures are the first information that is usually derived from refraction surveys and represent the most basic information about inhomogeneity in the crust. Using information about velocities of various types of rocks under *in situ* conditions, Christensen and Mooney (1995) developed models for the average composition of the tectonic provinces. They argue that the average P-wave velocity of the crust is 6.45 km/s and the average for the upper mantle is 8.09 km/s.

2.4.2 Reflection Surveys

Due to the widespread use by the petroleum industry, data from reflection surveys make up a majority of the data collected for imaging the earth's crust. In typical industry surveys, each source location is recorded by several tens of thousands of receivers. Source locations at sea can be as closely spaced as 30 m, and surface areas of the scale of several hundred km^2 can be surveyed. Generally, reflection data are processed using a method known as migration (Schneider 1978), which is an approach to back-propagate the wavefield measured at the surface to develop an image of the reflectivity of the earth's subsurface. An excellent review paper on modern methods for doing imaging using seismic reflection data is Etgen et al. (2009).

Migration is based on the representation theorem for scalar waves (see Schneider 1978) by using reciprocity, which shows how to relate known values of the wavefield on a surface S bounding a medium to the wavefield at any point interior to the surface:

$$u\left(\mathbf{x},t\right)=\int_{-\infty}^{\infty}dt'\oint_{S}dS\left(\mathbf{x}'\right)\left[-G\left(\mathbf{x},t;\mathbf{x}',t'\right)\mathbf{n}\nabla' u(\mathbf{x}',t')\right.$$
$$\left.+u\left(\mathbf{x}',t'\right)\mathbf{n}\nabla' G\left(\mathbf{x},t;\mathbf{x}',t'\right)\right], \tag{2.19}$$

where $u(\mathbf{x},t)$ is the wavefield at location $\mathbf{x}$ interior to S and at time t, $u(\mathbf{x}',t')$ is the wavefield at point $\mathbf{x}'$ on the surface S, $\mathbf{n}$ is the outward pointing unit normal vector to the surface, and ∇' is the derivative with respect to $\mathbf{x}'$ on the surface. Function $G(\mathbf{x},t;\mathbf{x}',t')$ is the Green's function for a source located at $\mathbf{x}'$ at time t' with a receiver located at $\mathbf{x}$ at time t. Since we know the wavefield near the earth's surface from measurements, we choose a Green's function that vanishes at the surface, and we obtain the migration integral for reflection data:

$$u(\mathbf{x},t)=\int_{-\infty}^{\infty}dt'\oint_{S}dS\left(\mathbf{x}'\right)u(\mathbf{x}',t')\mathbf{n}\nabla' G\left(\mathbf{x},t;\mathbf{x}',t'\right). \tag{2.20}$$

Equation (2.20) needs boundary and initial conditions. The boundary condition at the surface is the observed seismic data. At other boundaries, we use a radiation condition that states that the wavefield goes to zero at infinity. The initial condition is the causality condition that limits the time integral from time zero to some finite time. Physically, (2.20) allows us to predict the scattered wavefield below the surface of the earth. To obtain a reflection image of a velocity discontinuity, we use a simple imaging concept. We take the scattered wavefield just above a virtual reflector at the time it takes to propagate wavefield from the source to the reflector and back to the receiver.

In general, the Green's function for (2.20) has no analytic representation. Two popular numerical techniques to compute the Green's function consist of solving a finite difference representation of the scalar wave equation or solving the eikonal equation to obtain an asymptotic ray equation solution. The finite difference solution can be used to propagate the wavefield at the surface backward in time and into the earth; this is called reverse time migration. The formal limit of resolution of seismic migration for wavelength λ_w is given by $\delta r = \lambda_w/4$ (Claerbout 1985). Chen and Schuster (1999) give examples illustrating resolution that can be obtained with reflection imaging.

Figure 2.12 shows a 2-D cross section through a synthetic model developed to represent the earth's structure in a typical region of the Gulf of Mexico where salt features are common (Fehler 2008). In the Gulf region, the velocity through salt is dramatically higher than that of the surrounding strata, and the interface between the salt and the strata is irregular and often steeply dipping. The scattering by the salt results in extremely complicated seismograms during reflection profiling. Figure 2.13 shows a synthetic seismogram calculated using 3-D finite differencing of the variable-density acoustic wave equation for the 3-D model (e.g. Fehler 2010). Note the complexity of the seismogram calculated for this structure.

On a larger scale, observations of earthquake waveforms have provided evidence for reflected phases in the earth's crust. One notable observation of reflections,

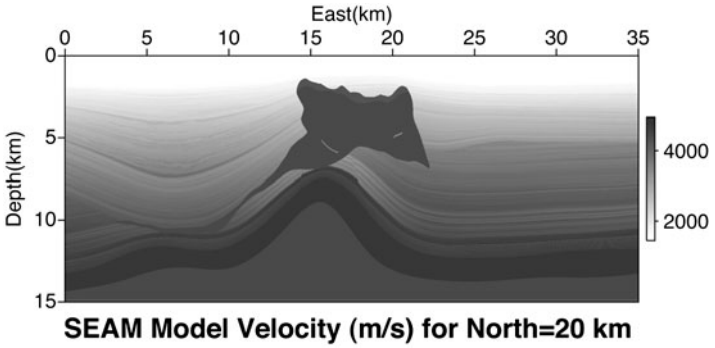

Fig. 2.12 Slice through a 3-D model of region containing a salt body that is typical of petroleum-bearing regions in the U.S. Gulf of Mexico. The velocity through the salt is as much as a factor of three times that of the surrounding strata. (Fehler 2008, copyright by the Society of Exploration Geophysics)

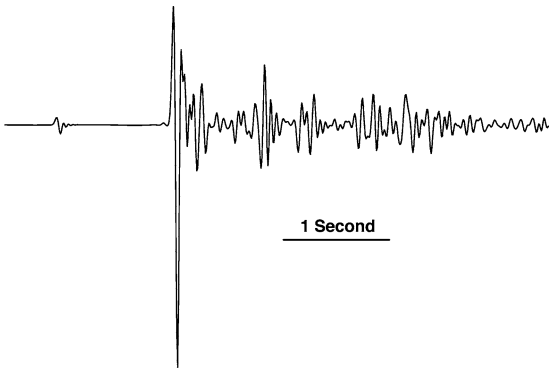

Fig. 2.13 Synthetic seismogram calculated using 3-D finite difference solution of the variable density acoustic wave equation for the salt model whose cross section is shown in Fig. 2.12. Shot and receiver are located on the earth's surface (in water) above the location of the salt body. Data are calculated as in Fehler (2010)

interpreted as coming from a mid-crustal reflector near Socorro, New Mexico, U.S.A. was made by Sanford and Long (1965) and later refined by Hartse et al. (1992). A waveform from an earthquake showing the reflected phases is shown in Fig. 2.14. Extensive investigation of the reflected phases has led to the conclusion that the reflections are caused by a mid-crustal magma intrusion that is perhaps as thin as 60 m, located at a depth of 19 km, and covering an area as large as 1,700 km^2 (Hartse et al. 1992). The existence of S-wave reflectors in the mid-crust was also reported to be associated with the Nikko–Shirane volcano in northern Kanto, Japan (Matsumoto and Hasegawa 1996).

In many continental regions, sequences of reflections are often observed from the lower crust and the vicinity of the Moho. The surveys show that the lower continental crust is heterogeneous compared with upper crust and the upper mantle as shown in Fig. 2.15. Warner (1990a) discusses the amplitudes of these reflections and indicates that some data show as many as 40 strong spatially consistent reflectors in 200 km-long 2-D seismic lines. Such spatially consistent and strong reflectors are not observed at shallow or mid-crustal depths. Warner (1990a) argues

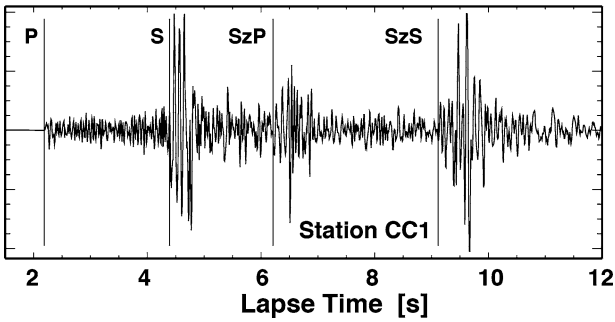

Fig. 2.14 Seismogram from an earthquake located near Socorro, New Mexico, U.S.A., where lapse time is measured from the earthquake's origin time. Phases SzP and SzS are phases reflected from a magma body located in the mid-crust. (Data courtesy of H. Hartse, A. Sanford, and J. Knapp)

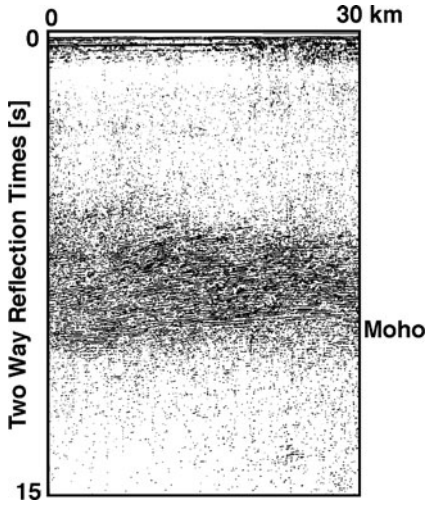

Fig. 2.15 Record section showing bright sub-horizontal layered reflections in the lower crust. The Moho is located at the base of the layering. (Warner 1990b, copyright by Elsevier)

that these reflectors are due to the intrusion of iron-rich mantle material into the silica-rich crust that flattens out into layers as it reaches a depth where the density contrast between the intrusion and the surrounding material no longer allows it to continue its ascent to the surface. To further investigate the sequence of reflections observed from the lower crust, Holliger et al. (1993) examined geological maps of a region of northern Italy that is considered an outcrop of material that was once in the lower crust. They estimated the spatial variations of material properties by comparing geological units with seismic velocities measured on rocks from the region and developed model sections for the lower crust. They used 2-D finite difference calculations to generate synthetic seismograms for the near and far offset seismic response for a region that contains a lower crust similar to the one developed from geological data. They found that the layered appearance of seismic data from

the lower crust may be explained by small scale (500–1000 m) spatial variation in material properties with maximum velocity variations of about 0.55 km/s against a flat background velocity of 6.3 km/s.

2.4.3 Receiver Function Method

Teleseismic P-waves recorded by seismic arrays are useful for deterministic imaging earth heterogeneity. For the incidence of teleseismic P-waves from bellow, S-waves are generated at the locations of velocity contrasts. Those P-to-S converted phases are recorded in the radial-component at the ground surface; however, the vertical-component P-wave is almost the same as the incident P-wave for near-vertical incidence. The receiver function method (Langston 1979) uses the deconvolution of the horizontal-component S-wave trace in the radial direction by the vertical-component P-wave trace for measuring the P-to-S conversion depth and the velocity contrast. The receiver function method has been widely used to reveal layered velocity structures.

Using an improved receiver function method based on the statistical multivariate autoregressive model, Shiomi et al. (2004) analyzed teleseismic waveform data recorded by the Hi-net in southwest Japan shown in Fig. 2.16a. Figure 2.16b shows the azimuthal dependence of estimated receiver functions at station OOTH in Shikoku, where time has been converted to depth. Remarkable phases, indicated with an arrow, appear at about 30 km in depth. A northward dip is seen in their azimuthal dependence: the phases for earthquake sources located in the back-azimuthal range 225–320° are slightly deeper than the other traces for back-azimuthal range 140–180°. Figure 2.16c shows density plot of the vertical section of the positive receiver function amplitude. Dark color indicates the location of the upper boundary of the high-velocity layer (the oceanic Moho) of the subducting Philippine Sea plate, which is dipping to northwest from Shikoku to Chugoku.

2.4.4 Velocity Tomography

Velocity tomography was introduced into seismology by Aki et al. (1976, 1977), who showed how to use travel times from distant earthquakes recorded on a closely spaced network of seismometers to determine the 3-D velocity structure of the region beneath the network. Subsequently, Aki and Lee (1976) and Crosson (1976) showed how to use travel times of local earthquakes recorded on a regional seismic array to simultaneously determine the 3-D velocity structure and earthquake locations. Since that time, velocity tomography has been widely used on regional and global scales with travel times from local and distant earthquakes to determine the P- and S-wave velocity structure of the lithosphere.

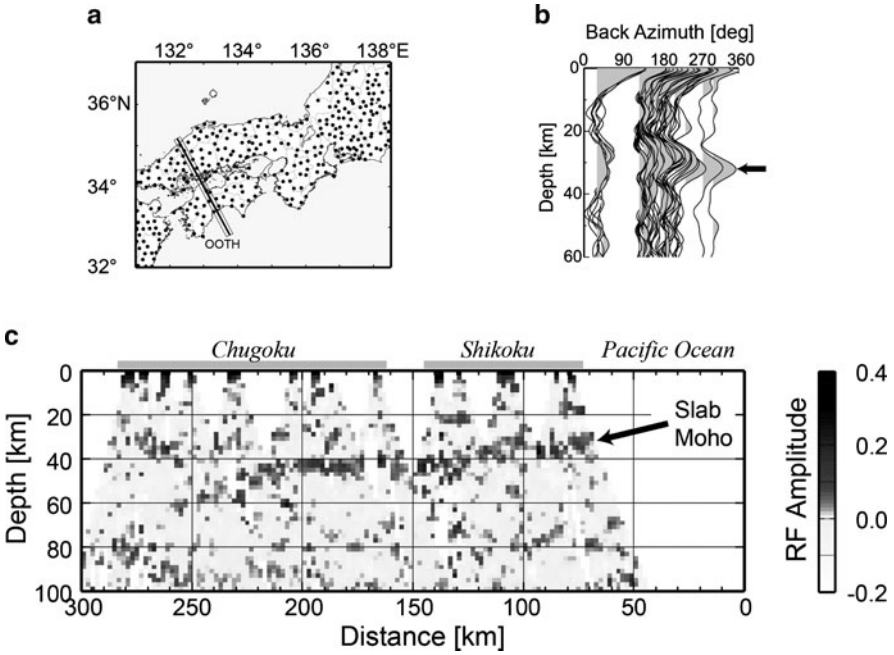

Fig. 2.16 (**a**) Hi-net stations of NIED and a northwest trending line in the Chugoku-Shikoku region, Japan. (**b**) Azimuthal dependence of the receiver function, where the ordinate is depth converted from time and the abscissa is back azimuth. An arrow indicates the coherent phases corresponding to the oceanic Moho discontinuity. (Shiomi et al. 2004, copyright by the American Geophysical Union) (**c**) Density plot of the vertical section of the positive receiver function amplitude along the line shown in (**a**), where an arrow indicates the oceanic Moho of the subducting Philippine Sea plate. (Modified from Shiomi et al. 2008, copyright by Willey)

The basis of the travel-time tomography method is that travel time through a structure can be written as

$$t_{ij} = \int_{l_{ij}} p(\mathbf{x}) dl, \tag{2.21}$$

where t_{ij} is the travel time for source i to receiver j, l_{ij} is the travel path from source i to receiver j, $p(\mathbf{x})$ is the slowness (inverse velocity) at location $\mathbf{x}$ in the earth and dl is the infinitesimal line element. Since the predicted ray path is not known until the velocity structure is known, inversion of (2.21) for $p(\mathbf{x})$ using known t_{ij} is a nonlinear problem. Generally, solution proceeds by the following approach. An initial velocity structure is assumed and the travel times through that structure are calculated from

$$t_{ij}^0 = \int_{l_{ij}^0} p^0(\mathbf{x}) dl, \tag{2.22}$$

where $p^0(\mathbf{x})$ is the initial slowness , l_{ij}^0 is the travel path between source and receiver for this initial model, and t_{ij}^0 is the travel time along this initial path. The ray path and travel times can be determined by using ray-tracing methods, such as initial value approaches (Červený 1987), ray bending (Um and Thurber 1987), or solutions of the eikonal equation (Fei et al. 1995; Vidale 1988). Defining the difference between the measured travel time t_{ij} and t_{ij}^0 as the delay time δt_{ij}, we find that

$$\begin{aligned}\delta t_{ij} = t_{ij} - t_{ij}^0 &= \int_{l_{ij}} p(\mathbf{x}) dl - \int_{l_{ij}^0} p^0(\mathbf{x}) dl \\ &\approx \int_{l_{ij}^0} (p(\mathbf{x}) - p^0(\mathbf{x})) dl = \int_{l_{ij}^0} \delta p(\mathbf{x}) dl. \end{aligned} \tag{2.23}$$

We may solve (2.23) for perturbations in slowness that give a better fit to the observed data than the initial model. The basic assumption in deriving (2.23) is that the changes in the slowness model do not result in significant changes in the ray path. This assumption is good so long as the slowness perturbations are small. Equations of the form of (2.23) are known as Radon transforms, named after Radon who showed a formal inverse transform to find the slowness $\delta p(\mathbf{x})$ in the case that the rays follow straight lines (Radon 1917). As pointed out by Chapman (1987), (2.23) shows that the data δt_{ij} are obtained as an integral over the slowness and are thus smoother than the slowness. Inverting (2.23) for slowness involves computing derivatives of data, which are numerically unstable with seismic data. Thus, seismologists include various constraints in the solution for slowness, such as requiring the slowness to be spatially smooth. These constraints limit the resolution of the spatial variation in structure that can be found with travel-time tomography.

Deans (1983) discusses the problem of inverting Radon transforms using real data. In general, the inversion is nonunique due to the fact that data are not available over all paths l_{ij} in (2.23). The projection-slice theorem illustrates how available data may help to constrain a slowness model. For the 2-D case in which slowness variations are small enough that rays follow straight paths, consider that we have travel-time anomaly measurements $\delta t(r, \theta)$ along coordinate r at angle θ to the x-axis, where coordinate r is perpendicular to ray-paths that travel through the medium at angle $\theta + \pi/2$. In 2-D, the theorem can be written as $\delta \tilde{t}(k_r, \theta) = \delta \tilde{p}(k_r \cos\theta, k_r \sin\theta)$, where $\delta \tilde{t}$ stands for the 1-D Fourier transform of δt with respect to r and $\delta \tilde{p}$ for the 2-D Fourier transform of the slowness in the x-y space (see Menke 1984b, p. 178). The projection slice theorem states that the Fourier transform of the travel-time anomaly data along a line perpendicular to the ray-paths traveling through the structure is equal to a slice of the Fourier transform taken through the slowness model. We can thus think of the image as built up in the Fourier domain from slices of travel-time data for rays propagating at various angles through the structure. Since observations of seismic travel time can usually be made for only a limited range of propagation angles, we have limited constraints on the structure of the earth available from travel-time tomography.

When studying the earth, (2.23) is valid only if the ray path does not depart from the path calculated for the original, unperturbed slowness structure. Thus, an iterative approach is used to solve (2.23), and slowness is constrained to vary slowly during each iteration. In addition, when (2.23) is to be solved using data collected in the earth, the inversion for slowness is not a well posed problem. Parts of the velocity structure are overdetermined and, due to noise in the data, generally overdetermined with inconsistent data. Portions of the structure are also underdetermined due to the limited angle that waves propagate through the region of study. Various methods for solving equations like (2.23) can be found in Menke (1984b) or Tarantola (1987).

When interpreting results of tomography, we must consider the resolution limits. In deriving (2.23) we have assumed that seismic information propagates along rays that are infinitely narrow. Ray theory is a high-frequency approximation to the wave equation, and we know that it is not appropriate for finite wavelength waves. One approximate measure of the spatial resolution of tomography is given by a measure of ray width (Nolet 1987) $\delta r = \sqrt{Z\lambda_w/8}$, where δr is the minimum separation of two objects to be resolved, Z is the travel distance between source and receiver, and λ_w is the wavelength. We note that $\sqrt{Z\lambda_w}/2$ is the maximum radius of the first Fresnel zone. When the spatial structure reaches a certain level of complexity, scattering effects become important and travel-time tomography cannot be applied. Devaney (1982) introduced the concept of diffraction tomography or inverse scattering, which uses both the amplitude and phase of incident wave. Diffraction tomography is based on a comparison of the observed wavefield with a scattered wavefield that is calculated using the Born (or Rytov) approximation for the perturbed media. Devaney (1982) showed that resolution of features as small as a half wavelength is possible by using diffraction tomography. Wu and Toksöz (1987) examined the application of diffraction tomography to geophysical data sets. Williamson (1991) investigated the effects of scattering on travel-time tomography by calculating the scale at which images calculated with travel time and diffraction formulations begin to differ. He found that the images begin to depart significantly when structure has variations on a scale smaller than $\delta r = \sqrt{Z\lambda_w}$, which should be viewed as the limiting resolution of travel-time tomography imposed by scattering effects.

Tomography has been applied to study the velocity structure of the mantle (Vasco et al. 1994), regional lithospheric structures using teleseismic data (Weiland et al. 1995), regional structures using local earthquakes and explosions as sources (Pujol 1996; Thurber 1993), the small-scale structure of a man-made geothermal reservoir (Block et al. 1994), the small-scale structure of the region between two boreholes, and the structure near a borehole using surface seismic sources and borehole receivers in a configuration known as Vertical Seismic Profiling (VSP).

We show results from three studies in different scales. Figure 2.17 shows a horizontal slice through a 3-D S-wave velocity tomogram calculated by Block et al. (1994) using data collected at a geothermal site in New Mexico, U.S.A. Data from microearthquakes induced by hydraulic fracturing and small explosions were used in the analysis. Figure 2.18a shows a horizontal slice through a P-wave velocity tomogram constructed using joint inversion for tomography and earthquake locations in the vicinity of Parkfield, California by Zhang et al. (2009). The average

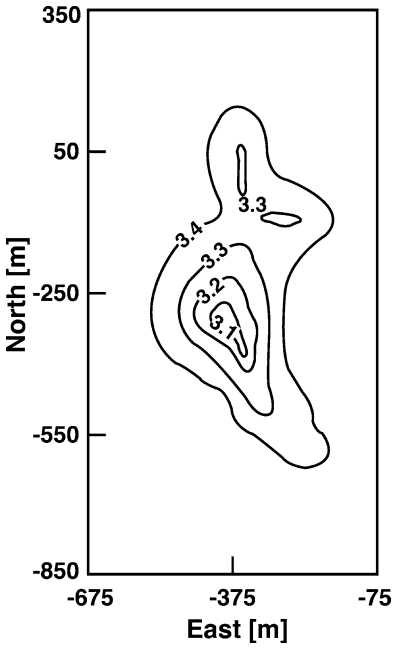

Fig. 2.17 Horizontal slice through a tomogram of S-wave velocity structure at depth 3500 m for the Fenton Hill hot dry rock geothermal energy site in New Mexico, U.S.A. Contours show velocity in km/s. Tomogram was calculated using travel times from microearthquakes induced by hydraulic fracturing in crystalline rock by Block et al. (1994)

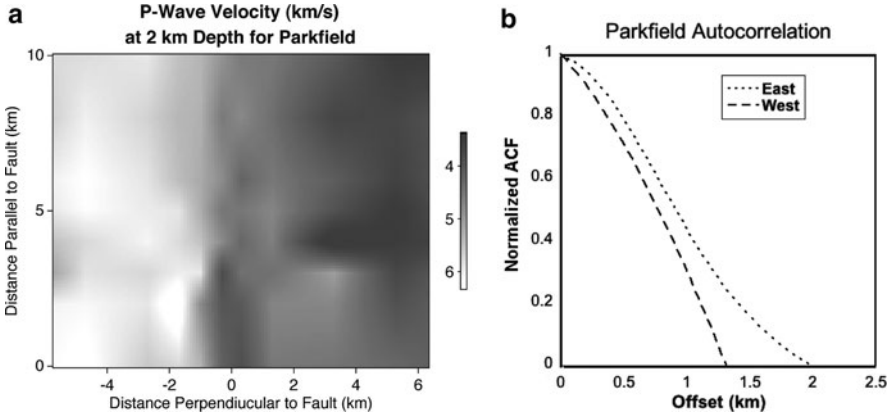

Fig. 2.18 (**a**) Horizontal slice through a velocity tomogram in the vicinity of Parkfield, California, where the vertical axis is roughly parallel to the San Andreas fault (SAF) and the horizontal axis is roughly perpendicular to the fault. The fault is located at position 0 on the horizontal axis. Density scale is shown on the right. (**b**) Normalized ACFs of the P-wave velocity fractional fluctuation in the west and east of the SAF. (Data courtesy of H. Zhang)

velocity in the east is clearly lower than that in the west of the San Andreas fault. Figure 2.19 shows a vertical cross section of S-wave velocity tomogram under northeastern Honshu, Japan. The subducting Pacific plate appears as a high-velocity zone and low-velocity bodies are found beneath active volcanoes (Zhao et al. 2009).

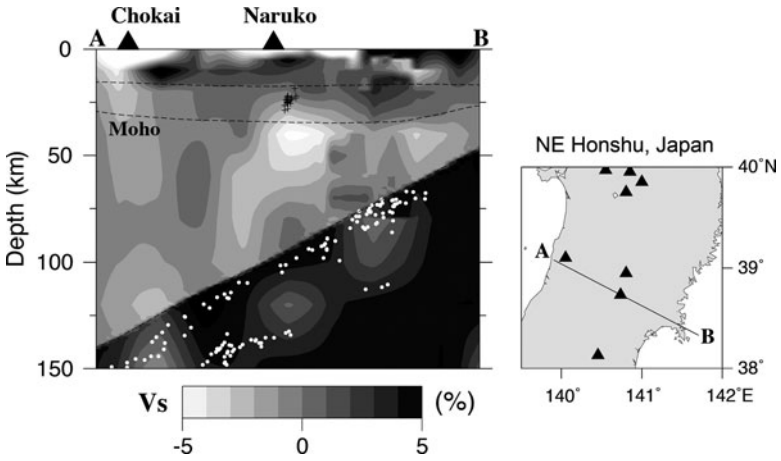

Fig. 2.19 Vertical cross section of the S-wave velocity tomogram beneath northeastern Honshu, Japan along a profile A-B as shown on the insert map. White and black colors denote low and high velocities, respectively. Black triangles denote active volcanoes. White dots denote intermediate-depth earthquakes that occur within the subducting Pacific slab. (Modified from Zhao et al. 2009, copyright by Elsevier)

In Sect. 2.3.2 we introduced the concept of ACF as a means of characterizing heterogeneity. Here, we investigate the ACF of velocity tomograms. This should be done with caution since artifacts introduced by the construction of tomograms may influence the autocorrelation. For example, tomograms are often constructed using constraints, such as a smoothing of the derived velocity model, to regularize the system of equations that must be solved to find the velocity model. In addition, the poor resolution of some portions of the model will lead to artifacts that influence the ACF. The normalized ACF $R(x)/\varepsilon^2$ of the fault-parallel P-wave velocity fractional-fluctuation in the Parkfield, California region is shown in Fig. 2.18b. The calculated ACF shows a shorter correlation length in the region West of the fault than in the region East of the fault.

It is desirable to compute the ACF directly from arrival-time data rather than from velocity models derived from travel-time data. Müller et al. (1992) developed a method for estimating the fractional fluctuation of medium slowness and correlation length from measurements of the ACF of travel times measured parallel to a wavefront. Using 2-D finite difference simulations, they tested the validity of their method and show that it is reliable when the ratio of seismic wavelength to correlation distance is less than about 0.5. Roth (1997) describes an extension of the method proposed by Müller et al. (1992) to the case that measurements are not made parallel to the wavefront. He tested the method using simulations and shows that it is reliable for cases where the propagation distances is less than about ten times the correlation distance. He applied the method to active seismic data collected

using air guns in the ocean off Sweden and found that the correlation distance is 330–600 m.

2.5 Scattering of High-Frequency Seismic Waves

High-frequency seismograms, which we take to mean higher than 1 Hz, contain features that reflect the random inhomogeneities in the earth. Traditionally, seismic networks record waveforms of local earthquakes with a bandwidth of about 1–30 Hz although recent instrumentation records higher frequencies. Recording of frequencies higher than about 30 Hz requires that the seismic sensor be placed in a borehole at depths below the highly attenuating surface layers to avoid cultural noise. When active sources such as explosions are used, frequencies as high as many kHz can be recorded, especially when both source and receiver are in boreholes.

In this section we will describe some of observed characteristics of seismograms of local and regional earthquakes that can be interpreted by using scattering models. We will briefly describe some of the approaches used in the modeling, which will be further developed in the following chapters.

2.5.1 Seismogram Envelopes

To characterize seismogram envelopes we often calculate the smoothed trace of the square of the seismogram, which is called the mean square (MS) seismogram envelope. Sometimes we take the square root of the MS trace to make the RMS seismogram envelope. In Fig. 2.20, we show a typical velocity seismogram of a small local earthquake (top), the corresponding RMS seismogram envelope (middle), and MS seismogram envelope (bottom). The direct S-wave is followed

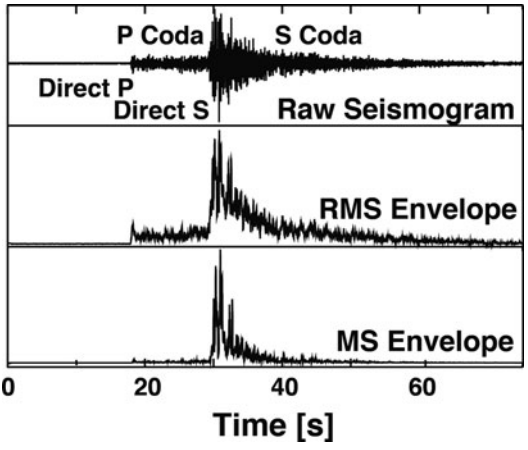

Fig. 2.20 Example of a velocity seismogram of a local earthquake and its envelopes

by wave trains whose phases look random but whose amplitudes decrease smoothly with increasing lapse time. These wave trains are called "S-coda waves," or simply "S-coda" or "coda." Initially the term "coda" was used to refer to the oscillations of the ground that continued after the passage of surface waves or the tail portion of a seismogram. Recently, this word has been used to refer to all wave trains except direct waves: "P-coda" for waves between the direct P- and S-arrivals and "S-coda" for waves following the direct S-arrival. The MS envelope, whose amplitude is linearly proportional to energy density, is appropriate for comparison with the synthesis based on the radiative transfer theory. On the other hand, the RMS envelopes reflect the visual image of the seismograms themselves.

For the analysis of seismograms recorded on paper, one can draw an envelope that is a connection of peaks of oscillating signals. For the analysis of digital seismograms, it is more convenient to use bandpass filters or Hilbert transform to calculate the envelope of coda waves. Applying a bandpass filter having a central frequency f with band-width Δf to a wave trace $v(t)$, we have the band-pass filtered trace $v(t, f)$. Taking the moving average of the square of v, we have the MS trace (envelope) of v as

$$\langle v(t, f)^2 \rangle_T = \frac{1}{T} \int_{t-T/2}^{t+T/2} \left| v\left(t', f\right) \right|^2 dt', \tag{2.24}$$

where T is a smoothing time constant. Taking the square root of the MS trace, we have the RMS trace as $\sqrt{\langle v(t, f)^2 \rangle_T}$. When v is the velocity of particle, a product of the mass density ρ_0 and $\langle v^2 \rangle_T$ is twice the kinetic energy, which is the sum of the kinetic and potential energies for a stationary state. For the analysis of coda waves, we often use octave-width bandpass filters. If we take a smaller band width, the time variation of MS trace usually shows more rapid oscillation. The smoothing time constant T is usually chosen to be twice the central period $2/f$ or larger.

When the bandpass filtered trace $v(t, f)$ is written in the Fourier integral as

$$v(t, f) = \frac{1}{2\pi} \int_{-\infty}^{\infty} \hat{v}(\omega, f)\, e^{-i\omega t} d\omega, \tag{2.25}$$

then the Hilbert transform is given by

$$\mathscr{H}[v(t, f)] = \frac{1}{2\pi} \int_{-\infty}^{\infty} \hat{v}(\omega, f)\, e^{-i\omega(t + |\pi/(2\omega)|)} d\omega. \tag{2.26}$$

There is a phase difference of $\pm\pi/2$ between the given wave trace and its Hilbert transform. The envelope that is tangent to successive peaks of oscillating waves is given by $\sqrt{|v(t, f)|^2 + |\mathscr{H}[v(t, f)]|^2}$. The MS trace defined by (2.24) is written as

$$\langle v(t, f)^2 \rangle_T = \frac{1}{2} \left\{ |v(t, f)|^2 + |\mathscr{H}[v(t, f)]|^2 \right\}. \tag{2.27}$$

2.5.2 S-Coda Waves

2.5.2.1 General Characteristics

The most prominent evidence for small scale random heterogeneities in the lithosphere is the appearance of coda waves on seismograms. On typical seismograms of local earthquakes, like those illustrated in Fig. 1.1, the direct S-wave is followed by S-coda. Direct S-wave amplitude decreases with increasing epicentral distance; however, average S-coda amplitudes, for example, those at lapse time of 100 s, have nearly equal amplitudes irrespective of epicentral distance. Rautian and Khalturin (1978) studied amplitudes of bandpass-filtered seismograms for a wide range of lapse times. They found that amplitudes of the early portions of seismograms are different from station to station; however, coda amplitudes have a common shape at all the stations after about two times and always after three times the S-wave travel-time from the source to the station. Figure 2.21a shows RMS envelopes measured from bandpass-filtered seismograms at two stations for a local earthquake in Central Asia, where the station separation is about 45 km. The figure shows the similarity of the shape of the late coda portion of the envelope at the two stations. Figure 2.21b shows coda amplitude vs. lapse time for a suite of small earthquakes in Kanto, Japan recorded at a station in Tsukuba (1978). The similarity of the curve shape for all the earthquakes is clear.

S-coda characteristics are clearly seen in recent digital recordings having a wide dynamic range. Figure 2.22 shows RMS envelope traces of a small earthquake at different epicentral distances in Tohoku, Japan, where the logarithmic plot is used for amplitude. Although direct wave amplitude decreases roughly with increasing travel distance, we see a smooth common decay curve with increasing lapse time for coda envelopes irrespective of epicentral distance.

Figure 2.23 shows a comparison of vertical- and horizontal-component S-coda envelopes of a small local earthquake. There is little difference between envelopes for the two components of motion recorded at either a borehole site (a) or a surface site (b).

2.5.2.2 Duration Magnitude

The magnitude of a local earthquake is often determined from the average of the maximum amplitudes measured at many stations surrounding the epicenter after a distance correction is applied at each station. The magnitude calculated from amplitudes has been found to be proportional to the logarithm of the F-P duration time of a local seismogram, t_{F-P} in second, which is the length of time measured from the P-wave onset to the time when the S-coda amplitude decreases to the level of microseisms or noise (Solov'ev 1965; Tsumura 1967). The proportionality is shown in Fig. 2.24a, where earthquake local magnitudes determined from measurements of amplitude by the Japan Meteorological Agency

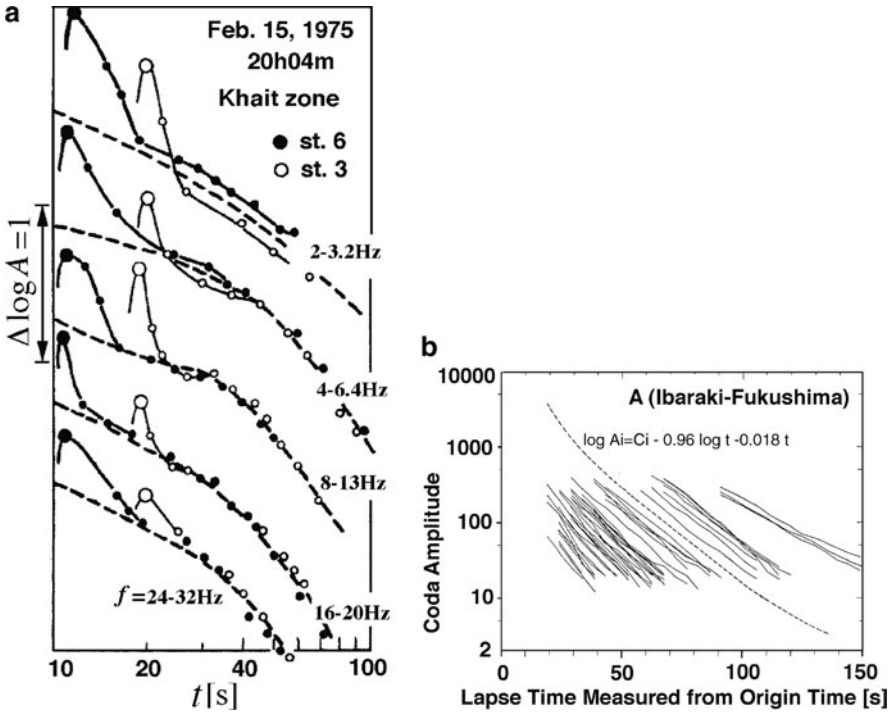

Fig. 2.21 (**a**) Log-log plot of RMS seismogram envelopes vs. lapse time measured from the origin time for different frequency bands for an event recorded at two stations having different epicentral distances in Central Asia, where closed and open circles are direct S-arrivals. (Rautian and Khalturin 1978, copyright by the Seismological Society of America) (**b**) Semi-log plot of RMS coda-amplitude decay with lapse time measured from the origin time for local earthquakes of the 6 Hz-band recorded at Tsukuba in Kanto, Japan, where a broken curve is the average decay curve. (Tsujiura 1978, copyright by the Earthquake Research Institute, the University of Tokyo)

(JMA) are plotted against the F-P duration time at station Wakayama in Japan, where F-P times were visually read from paper seismograms (Tsumura 1967). The regression line is $M_{JMA} = -2.36 + 2.85 \log t_{F-P}$. Figure 2.24b shows a plot of M_{JMA} against (F-P) duration time read by a computer at a station in Kanto, Japan. The regression line is $M_{JMA} = -2.50 + 3.25 \log t_{F-P}$, where the standard deviation is 0.31 and the correlation is as large as 0.9 (Tatsukawa 1983). The logarithm of duration time has been used for the quick determination of earthquake magnitude in many regions of the world. This correlation between magnitude and the logarithm of duration time is consistent with the similarity in shape of the later portion of seismograms observed at regional seismic stations and the conclusion that coda portions of seismograms are composed of scattered waves.

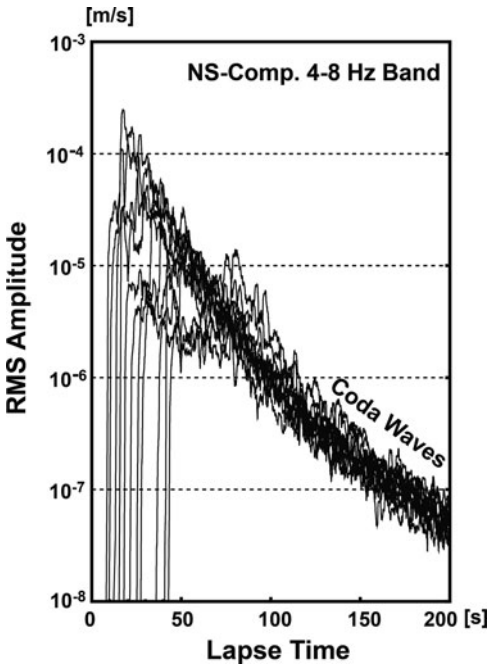

Fig. 2.22 RMS envelopes of an M 4.8 earthquake of at different epicentral distances in Tohoku, Japan registered by Hi-net (NIED), where each vertical line shows the P-wave onset. (Sato and Fehler 2007, copyright by Elsevier)

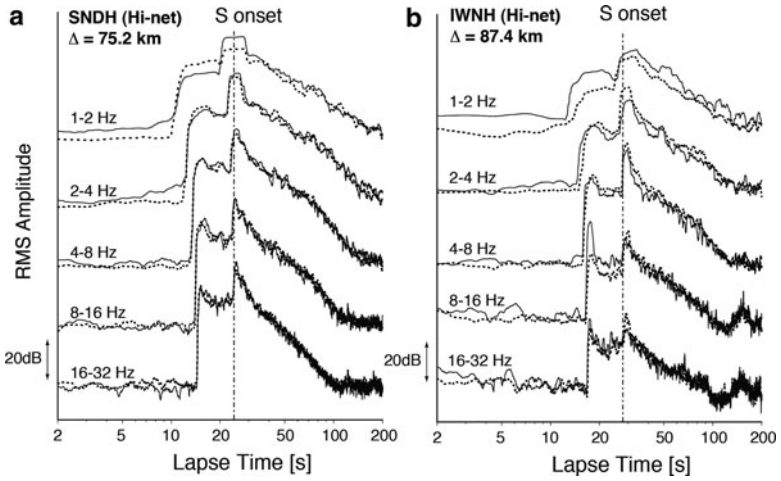

Fig. 2.23 Comparison of UD-component (solid) and NS-component (dotted) RMS envelopes of a small earthquake: (**a**) Borehole site SNDH and (**b**) surface site IWNH of Hi-net (NIED)

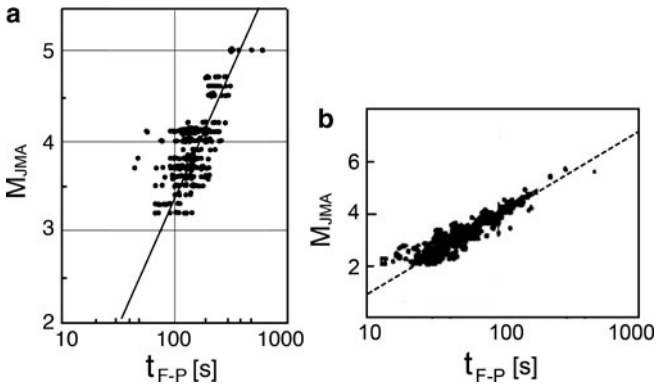

Fig. 2.24 Relationship between the magnitude M_{JMA} determined by using amplitude data and the F-P duration time at a single station. (**a**) At ERI station Wakayama, Japan. (Tsumura 1967, copyright by the Earthquake Research Institute, the University of Tokyo) (**b**) At station ASG of NRCDP (NIED) in Kanto, Japan. (Tatsukawa 1983, copyright by National Research Institute for Earth Science and Disaster Prevention, Japan)

2.5.2.3 Array Analysis of Coda

Frequency–Wavenumber Analysis

The nature of coda waves has been studied by using array observations. Aki and Tsujiura (1959) analyzed correlations of seismograms among six vertical-component seismographs deployed on granitic rock at the foot of Mt. Tsukuba in Kanto, Japan and reported that there was little energy at the receiver array that had left the epicenter region of the earthquake as plane waves. One way to find the propagation direction of component waves using array observations is to use a frequency–wavenumber power spectrum. For a stationary time series $u(\mathbf{x}, t)$, we define the frequency-wavenumber (f–$\mathbf{k}$) power spectral density as the Fourier transform of the autocorrelation function $\langle u(\mathbf{x}, t)\, u(\mathbf{x}+\mathbf{x}', t+t')\rangle$ (Lacoss et al. 1969):

$$P_{\mathrm{fw}}(\mathbf{k}, f) = \iiint_{-\infty}^{\infty} \left\langle u(\mathbf{x}, t)\, u\left(\mathbf{x}+\mathbf{x}', t+t'\right)\right\rangle e^{-i(\mathbf{k}\mathbf{x}'+2\pi f t')} d\mathbf{x}' dt'. \tag{2.28}$$

For wavefield data having a finite duration in a given frequency band having center frequency f, we usually make a contour plot of the estimated f–$\mathbf{k}$ power spectral density P_{fw} in the k_x–k_y plane. A peak in the plot indicates the direction of approach and the apparent propagation velocity (slowness) of the plane wave that coherently crosses the array. Figure 2.25 shows results of an f–$\mathbf{k}$ analysis of data recorded by an eight-element seismic array located SE of the center of the Valles Caldera in northern New Mexico, U.S.A. The analysis was performed on narrow-band filtered data from three 2 s time windows, one surrounding the direct P-arrival, one surrounding the direct S-arrival, and one beginning 20 s after the direct S-arrival

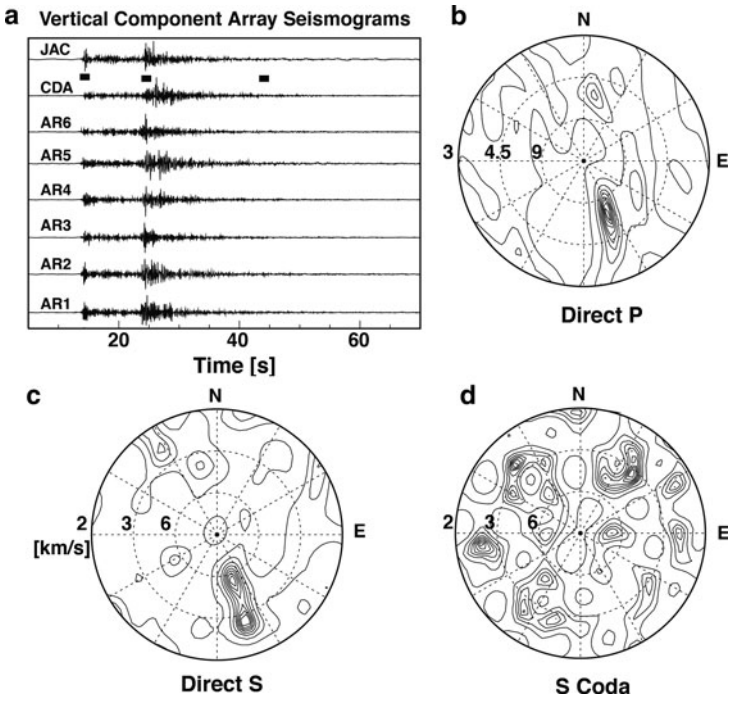

Fig. 2.25 (**a**) Vertical-component seismograms recorded by an eight element array located in the Valles Caldera, New Mexico, U.S.A. of a small local earthquake located at a distance approximately 80 km SSE of the array, where bold bars indicate 2 s long time windows used for f–**k** analyses. (**b**) f–**k** power spectrum of vertical-component data surrounding the direct P-arrival shown by the contour plot in the slowness space. Data were filtered into the 2–5 Hz frequency band prior to analysis. Numerals inside circle refer to velocity of waves crossing the array. (**c**) f–**k** power spectrum of EW-component data surrounding the direct S-arrival. Frequency band is 1.3–3 Hz. (**d**) f–**k** power spectrum of EW-component S-coda data beginning 20 s after the direct S-arrival. Frequency band is 1.3–3 Hz

in coda. As shown by contour plots in the slowness space in Fig. 2.25b and c, the f–**k** power spectrum of waveform data that includes the direct waves shows that the direct waves are dominated by waves arriving from the direction of the event indicated by the peaks in the SSE portion of the plots. The S-coda, on the other hand, shows no consistent arrival direction, as shown by Fig. 2.25d, where high amplitude contours appear with apparent velocity of about 3 km/s in all quadrants of the plot.

Spudich and Bostwick (1987) proposed to use seismograms recorded at a single station for a cluster of earthquakes as a virtual seismic array. Source and receiver positions are exchangeable because of the source-receiver reciprocity of the Green's function of elastodynamics, so the earthquake cluster can be considered an array of seismic stations within the earth that records seismograms from a single source located at the position of the real seismic receiver that recorded the earthquakes. Making the f–**k** analysis of a set of aftershocks of the 1984 Morgan Hill, California

earthquake, they measured the propagation directions and slownesses of those component waves as they travel through the earthquake focal region. The early S-coda, starting immediately after the direct S-wave and ending at twice the S-wave travel-time, was dominated by waves that are multiply scattered near the station since the propagation direction is upward and almost the same as the direct S-wave. Using the same method, Scherbaum et al. (1991) analyzed microearthquake clusters in northern Switzerland. The f–$\mathbf{k}$ analysis plots show two different patterns: early coda immediately following the direct S-wave was composed of wavelets leaving the source region with the same slowness vector as the direct S-waves; however, latter S-coda waves are composed of wavelets leaving the source region in a variety of directions. The transition between the two types often takes place at $1.5 \sim 2$ times the S-wave travel-time from source to receiver.

Semblance Analysis

Semblance is another measure of the coherency of waves. Semblance coefficient is defined as

$$S_c(t, \mathbf{p}) = \frac{\sum_{j=K(i)}^{K(i)+N} \left[\sum_{i=1}^{M} u\left(\mathbf{x}_i, t_j\right) \right]^2}{M \sum_{j=K(i)}^{K(i)+N} \sum_{i=1}^{M} u\left(\mathbf{x}_i, t_j\right)^2}, \tag{2.29}$$

where M is the number of stations and N the number of samples (Neidell and Taner 1971). When the aperture of the array is small and we may consider the waves as plane waves, we may set the starting time of the window as $K(i) = t + \mathbf{p}\mathbf{x}_i$, where $\mathbf{x}_i$ is the coordinate of the i-th station, $\mathbf{p}$ the apparent slowness in 2-D, and t the arrival time at the center of array. Semblance may be viewed as the ratio of the power of the stacked beam to the product of the total power in the traces and the number of channels M.

Kuwahara et al. (1997) evaluated semblance coefficients using array observations of microearthquakes in Kanto, Japan to analyze propagation characteristics of waves. Figure 2.26 shows an example of the temporal variation of arrival azimuth, slowness, and the semblance coefficient for vertical-component seismograms of a local earthquake registered by a seismic array, which is composed of 13 seismometers with natural frequency of 2 Hz. Results show that the P-coda has almost the same propagation direction and apparent velocity as those of the direct P-wave that arrives from the direction of the epicenter (see also Wagner and Owens 1993). The slownesses for S-coda are generally larger than those for P coda. The semblance coefficient for the P-coda is quite high, but it rapidly drops in the S-coda. It means that the S-coda is composed of waves with widely distributed propagation directions and low semblance coefficients.

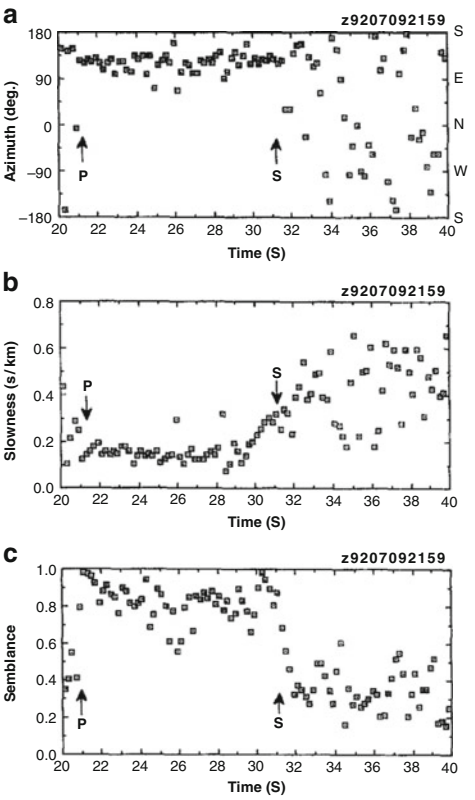

Fig. 2.26 Arrival azimuth (*top*), slowness (*middle*) and semblance coefficient value (*bottom*) vs. time for a local earthquake in Kanto, Japan determined from the semblance analysis of vertical-component data recorded by a seismograph array, where the time window length is 0.2 s. (Kuwahara et al. 1997, copyright by Elsevier)

2.5.2.4 Basic Models for S-Coda and Scattering Attenuation

The above observations strongly suggest that high-frequency coda waves are incoherent and their propagation directions are omni-directional. To explain the observed smooth temporal decay of coda amplitude that is independent of epicentral distance, Aki and Chouet (1975) proposed a model in which S-coda is composed of S-waves that have been scattered by heterogeneities distributed in a large region outside the zone containing the direct wave path from the source to the receiver. Reverberations in soft layers or the trapping and release of seismic energy by lakes or ponds cannot explain the observed characteristics. There have been developments in modeling coda on the basis of scattering by a random distribution of heterogeneities. We will introduce observation of coda waves and basic scattering models in Chap. 3. If we consider that S-coda wave excitation is dominated by scattering of S-waves from heterogeneities in the earth, conservation of energy says that the energy is supplied from the direct S-wave. The importance of scattering attenuation was pointed out by Aki (1980a) and theoretical models were proposed by Wu (1982a,b) and Sato (1982a,b).

Chapter 4 will introduce the scattering theory on the basis of the Born approximation for waves in random media. Chapter 5 will give a model for the attenuation

caused by scattering in randomly inhomogeneous elastic media. Hoshiba et al. (1991) and Fehler et al. (1992) proposed the multiple lapse time window analysis for the quantitative measurement of scattering loss and intrinsic absorption from the whole S-seismogram envelopes on the basis of the multiple isotropic scattering model, which will be introduced in Chap. 8.

2.5.3 Three-Component Seismogram Envelopes

Three-component seismograms of a local earthquake starting from the P-wave onset until the end of the S-coda reflect not only the source process characterized by the fault-plane geometry and the source-time function but also the scattering characteristics of the heterogeneous lithosphere. As an example, Fig. 2.27 shows typical three-component seismograms recorded at five stations having epicentral distances between 10 and 60 km located in the vicinity of the Izu Peninsula, Kanto, Japan. The earthquake source is a strike slip type. P-wave first motions are shown on the lower hemisphere projection in the middle of the figure. Appearance of S-coda is common to all seismograms; however, we find considerable spatial variation in the amplitude envelopes of the P and S-codas that are functions of both source-receiver azimuths and hypocentral distances. At station NRY, located near the P-wave nodal line, the direct P-phase is unclear on the vertical-component and the S-phase is a large pulse having a period of 0.2 s on the NS-component. The P-coda amplitude gradually increases with time on all three components, and the maximum peak amplitude of the S-phase on the vertical-component occurs a little later than those on the horizontal-components. At stations YMK, SMD and JIZ located near the maximum P-wave radiation directions, the direct P-wave is dominated by one pulse having a period of 0.2 s on the vertical-component. P-coda envelopes are concave between the P- and S-phases, decreasing with increasing time after the direct P-arrival.

There is a typical example how seismic waves are distorted by scattering as frequency increases. The 2000 western Tottori, Japan earthquake was a strike-slip earthquake whose seismic signals were recorded by stations surrounding the mainshock epicenter. Takemura et al. (2009) analyzed horizontal-component seismograms of the mainshock and aftershocks. Figure 2.28 shows the azimuthal variation for two frequency bands of the maximum transverse-component S-wave amplitude plotted on the circle at a reduced distance. The observed amplitudes for the 0.5 Hz band (solid lines and dots) are in harmony with the theoretical radiation pattern of the point shear dislocation source (broken lines); however, the coincidence becomes poor and the observed radiation pattern approaches to an isotropic radiation for the 5 Hz band. This result means scattering becomes stronger with increasing frequency.

Modeling the wave trains of P- and S-codas as incoherent singly scattered waves, we may sum up the scattered waves' power and synthesize the whole seismogram envelope. We will introduce a method in Chap. 6 for synthesizing

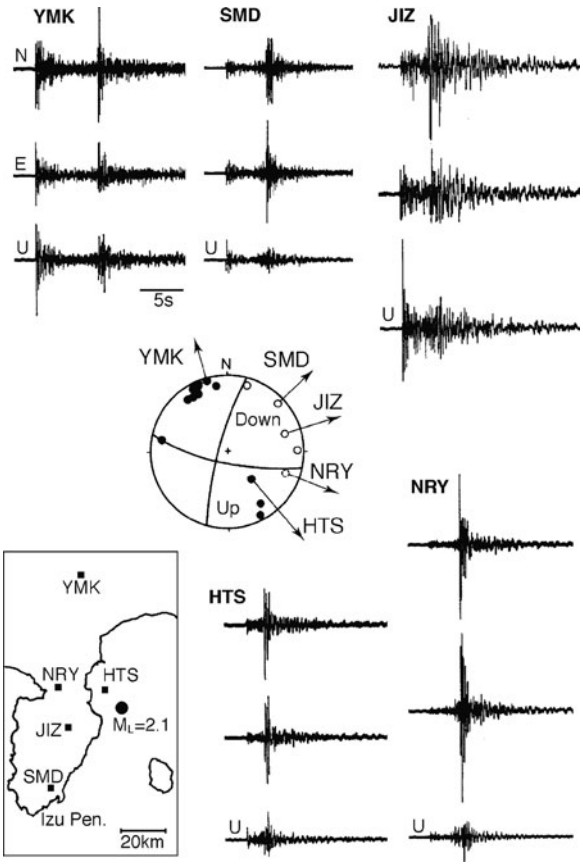

Fig. 2.27 Three-component seismograms of an M_L 2.1 microearthquake at 12.7 km in focal depth (closed circle on the map) recorded near the Izu Peninsula, Japan at five stations (solid squares), where the amplification gains are the same for three components at each station. Initial P-motions are plotted on the lower hemisphere. (Sato 1991a, copyright by Elsevier)

three-component seismogram envelopes by using single scattering amplitudes from the Born approximation for elastic waves. Envelope synthesis in the multiple scattering regime will be presented in Chap. 8 based on the radiative transfer theory.

2.5.4 Broadening of Seismogram Envelopes and Excitation of the Orthogonal-Component of Motion

2.5.4.1 Envelope Broadening of S-Waves

Another piece of evidence supporting the existence of heterogeneity in the lithosphere is the broadening of S-wave seismogram envelopes of earthquakes recorded

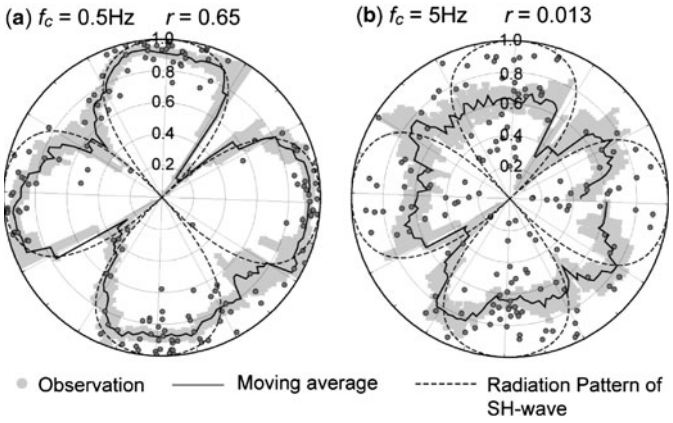

Fig. 2.28 Distribution of the maximum transverse-component S-wave amplitude at a reduced distance against azimuth from the fault strike for the (**a**) 0.5 Hz and (**b**) 5 Hz bands. Data are seismograms of mainshock and aftershocks of the 2000 western Tottori, Japan earthquake. Dots are observed amplitudes relative to the RMS amplitudes of 152 waveforms of 29 aftershocks. The solid lines illustrate their moving average, and the gray areas show the standard deviation. The theoretical radiation pattern for the SH wave is shown by broken lines. (Takemura et al. 2009, copyright by Willey)

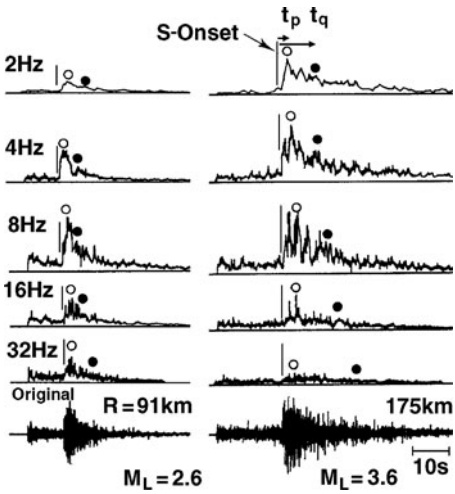

Fig. 2.29 RMS envelopes of bandpass-filtered seismograms (NS-component) of two earthquakes in southeast Honshu, Japan, recorded at station ASO of NRCDP. S-wave onset (vertical bar), arrival of the maximum peak (open circle), and the arrival of half-maximum amplitude (closed circle) are shown. (Sato 1989, copyright by the American Geophysical Union)

at long travel distances. The source duration of earthquakes having local magnitude less than 4 is shorter than 1 s as estimated from the empirical relationship describing the fault rupture process; however, Fig. 1.2 shows that the apparent duration time of the S-seismogram just after the direct S-arrival increases with increasing travel distance much longer than 1 s. Fig. 2.29 shows typical seismogram envelopes, recorded at a station in Kanto, Japan, of two earthquakes having different hypocentral distances. The maximum peak, indicated by an open circle on each bandpass-filtered

RMS seismogram, occurs several seconds after the S-wave onset that is indicated by a vertical bar. We also find a delay in the time of arrival of the half-maximum amplitude as indicated by a closed circle in Fig. 2.29. The wave that is initially an impulse at the source collapses and broadens with increasing travel distance. The seismometer is installed on hard rock; therefore, we can not attribute the envelope broadening to reverberation in shallow soft deposits. Increasing apparent duration is called "envelope broadening." It was initially proposed that S-wave seismogram broadening is due to strong diffraction and multiple forward scattering caused by slowly varying velocity structure. The envelope synthesis was modeled by employing the Markov approximation, which is a stochastic treatment of the parabolic approximation of the wave equation in random media (Sato 1989).

Analyzing S-wave envelopes of microearthquakes in Kanto–Tokai, Japan, where the Pacific plate is subducting from east to west, Obara and Sato (1995) found regional differences in observed envelope broadening. Most of earthquakes used for the analysis are associated with the subducting slab. Figure 2.30b shows examples of their bandpass filtered RMS traces at stations KGN and KIB for a deep focus earthquake *E* beneath the Izu Peninsula (see Fig. 2.30a). They found that envelope broadening is typically stronger for higher frequencies in records at KGN on the back-arc side of the volcanic front but weaker and frequency independent in

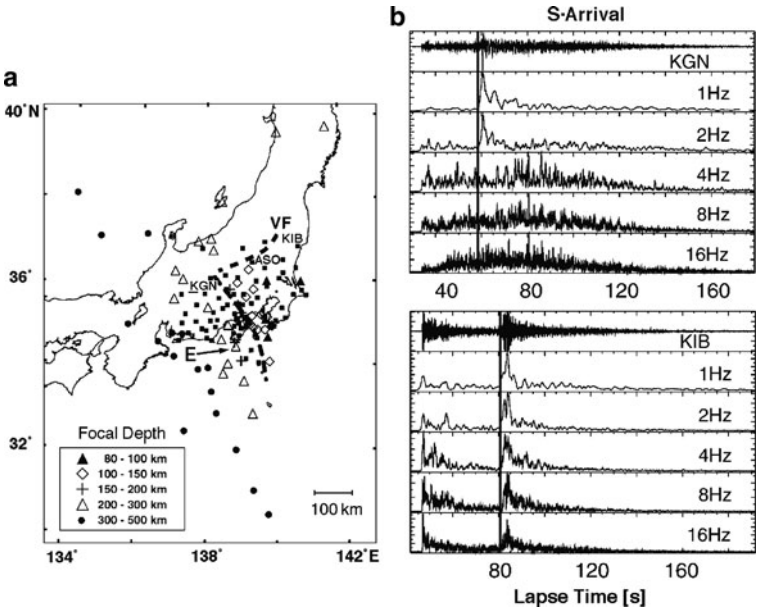

Fig. 2.30 (**a**) NRCDP (NIED) seismic stations KGN and KIB, and deep focus earthquake *E* in Kanto - Tokai, Japan. (**b**) Horizontal-component (EW) seismograms and their RMS octave-width bandpass-filtered traces at KGN and KIB for a deep focus event *E*, where each trace is normalized by its maximum RMS amplitude and a vertical bar indicates the S-wave onset. (Obara and Sato 1995, copyright by the American Geophysical Union)

records at KIB on the fore-arc side. The sharp boundary defined by the edge of the distribution of volcanoes running from north to south on the fore-arc side of Honshu, Japan is called the volcanic front (VF) (Sugimura 1960). The VF is located at the projection onto the surface of the 110 km iso-depth contour of seismicity associated with the subducting Pacific plate (Tatsumi 1986). Heat flow is lower east of the VF (fore arc side) and higher west of the VF (back arc side). Obara and Sato (1995) showed that these regional differences in envelope broadening mean that PSDF of velocity inhomogeneity is rich in short-wavelength components in the mantle wedge on the back-arc side and poor on the fore-arc side.

Later Takahashi et al. (2007) precisely examined how the peak delay from the S-wave onset depends on the ray path in northern Japan, which is shown in the inset of Fig. 2.31. They found that peak delays observed in the back-arc side of the VF are larger for rays which propagate beneath Quaternary volcanoes (see Fig. 2.31b and d); however, peak delays for rays which propagate between Quaternary volcanoes are as short as those observed in the fore-arc side of the VF (see Fig. 2.31a, c and e). Large peak delay suggests strong scattering due to medium inhomogeneity. Those observations mean that the velocity structure beneath Quaternary volcanoes is not only characterized by low velocity and large intrinsic absorption revealed from tomography studies but also characterized by strong random velocity inhomogeneities.

In Chap. 9, we will present the statistical mathematics for modeling envelope broadening in random media on the basis of the Markov approximation for the parabolic wave equation.

2.5.4.2 Nonisotropic Random Medium Oceanic Slab

Furumura and Kennett (2008, 2005) proposed that a subducting oceanic slab can be an efficient wave-guide when it consists of a random medium whose correlation distance across the width of the slab is shorter than that along the length of the slab. Figure 2.32a shows the configuration of the oceanic slab beneath an island arc, in which an earthquake of M_L 6 is placed. They numerically showed the existence of frequency-dependent propagation characteristics with a faster low-frequency phase followed by large-amplitude high-frequency signals having very long coda as shown in Fig. 2.32b. Multiple reflections along the slab direction are consistent with the intensity anomaly observed on the island arc for deep focus earthquakes that occur along the subducting oceanic slab.

2.5.4.3 Envelopes of Teleseismic P-Waves

When teleseismic P-waves propagate through a scattering layer, the primary wave loses energy due to scattering and intrinsic absorption, then the scattered energy appears as P-coda energy behind the P-wave front. From the analysis of vertical-component trace envelopes observed in the world, Korn (1993) found

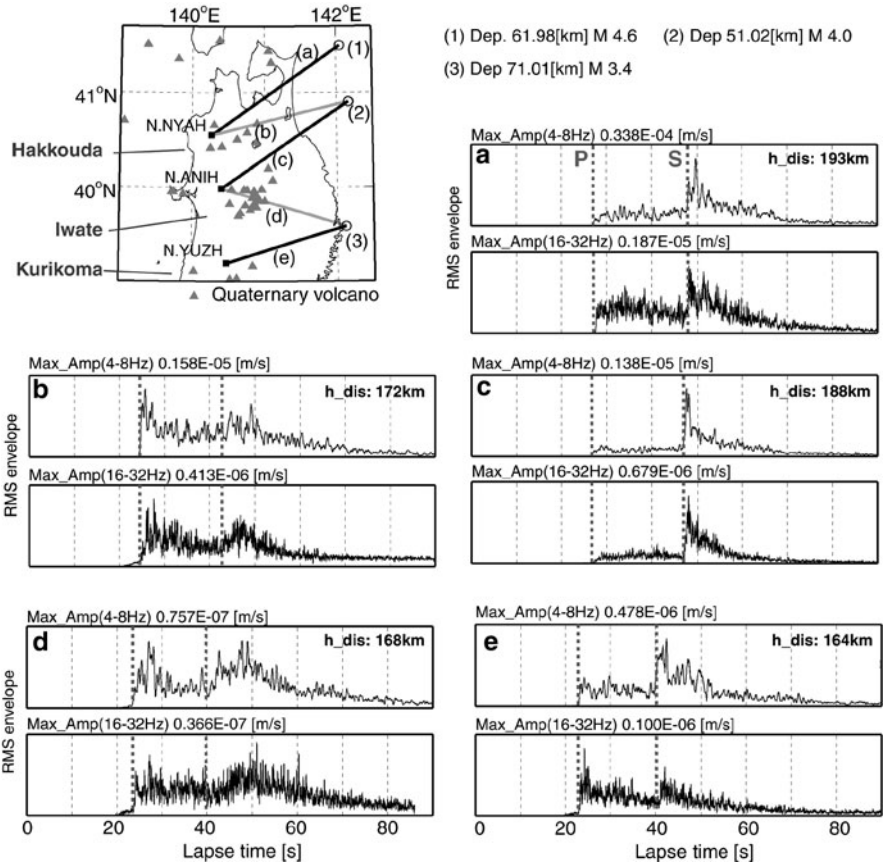

Fig. 2.31 (Map) Ray path dependence of S-wave peak delay from the S-onset, where open circles, closed boxes and gray triangles are earthquake epicenter, stations and Quaternary volcanoes, respectively. (**a**), (**c**) and (**e**) are bandpass filtered RMS velocity envelopes (NS-component) for rays traveling between Quaternary volcanoes, (**b**) and (**d**) are those for rays traveling beneath Quaternary volcanoes, where gray vertical broken lines are P- and S-onsets. (Takahashi et al. 2007, copyright by Willey)

regional difference in lithospheric heterogeneity: strong scattering at island arcs and smaller scattering on stable continental areas like Australia.

Shearer and Earle (2004) analyzed the envelope characteristics of P-wave and P-coda of teleseismic events. In Fig. 2.33, the top panels show peak P-wave amplitude versus epicentral distance and the bottom panels show stacks of P coda amplitudes at 1 Hz relative to the maximum P-wave amplitude for both shallow and deep focus earthquakes. P-wave amplitude versus distance is sensitive to the intrinsic attenuation in the mantle. Different from the S-wave envelopes of local earthquakes, there is no increase in the P-wave envelope width with increasing epicentral distance. To model these observations, Shearer and Earle (2004) found

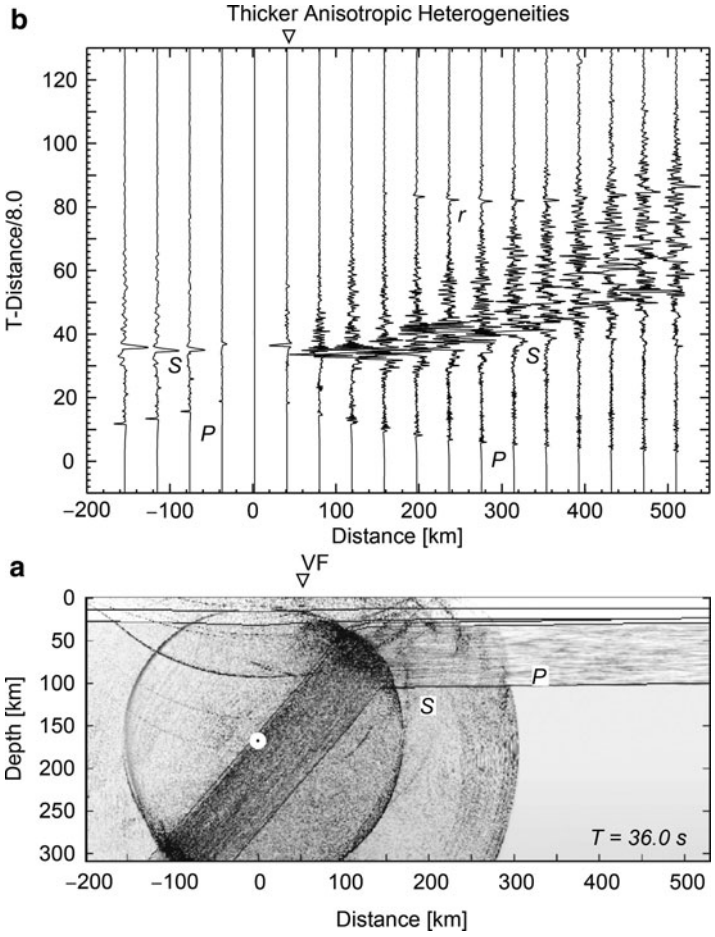

Fig. 2.32 (**a**) Snapshot of waves for an M_L 6 earthquake source in a nonisotropic random-medium oceanic slab sinking beneath an island arc, where VF means the volcanic front. (**b**) Synthesized velocity traces. (Furumura and Kennett 2008, copyright by Elsevier)

that scattering occurs mostly in the lithosphere and upper mantle but that a small amount of lower-mantle scattering was also required.

2.5.4.4 Excitation of the Orthogonal Component of Motion

When we examine the particle motion around the direct-wave arrival, we find evidence of scattering along the propagation path from the source to the receiver. The 3-D particle motion trajectory, which gives some information about the types of seismic waves and their directions of travel, can be analyzed by using the 3-D covariance matrix. In a homogeneous medium, the P-wave should be linearly polarized along the direction of travel and the S-wave is polarized in the plane

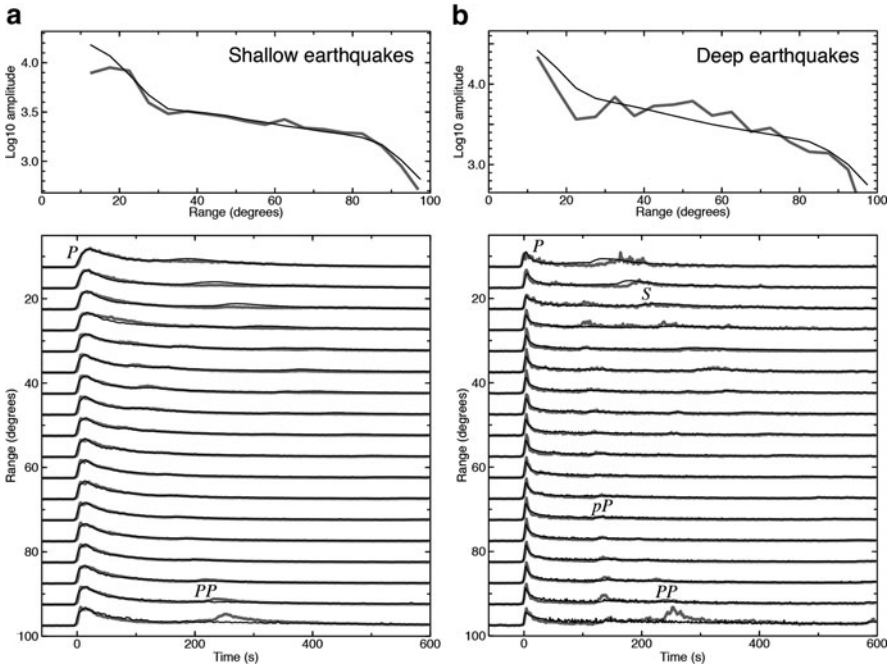

Fig. 2.33 Comparisons between envelope stacks of teleseismic P-wave arrivals (thick gray lines) with predictions of a Monte Carlo simulation for a whole-earth scattering model (thin lines). The left panel (**a**) shows results for shallow focus earthquakes ($\leq$50 km) and the right panel (**b**) for deep focus earthquakes ($\geq$400 km). The top panels show peak P-wave amplitude versus epicentral distance. The bottom panels show P-wave and P-coda envelopes vs. lapse time from the direct P-arrivals, where amplitudes are normalized by the energy in the first 30 s. (Shearer and Earle 2004, copyright by Willey)

perpendicular to the direction of travel. In most cases, the P-wave particle motion is observed to be elliptical, which indicates scattering. The aspect ratio of the ellipsoid, given by the square root of the ratio of the middle eigen value to the maximum eigen value of the covariance matrix composed of three-component data for a short interval of time around the P-wave, indicates the strength of scattering. If the aspect ratio is close to zero, the particle motion is needle-like indicating little scattering. On the other hand, if the ratio is close to one, the particle motion is spherical representing strong scattering.

Matsumura (1981) measured the ratios of eigen values for P-waves from seismograms of local earthquakes recorded at station IWT in Kanto, Japan, where a three-component velocity-type seismograph is installed in a borehole in pretertiary formation rock at a depth of 3510 m. The predominant frequency of the data is about 10 Hz, and no phases reflected from the free surface are included in the 0.8 s time window used for the analysis. He found differences in scattering strength for earthquakes occurring in different regions, as shown in Fig. 2.34, where scattering is stronger for earthquakes in the north than in the south. He found a similar pattern

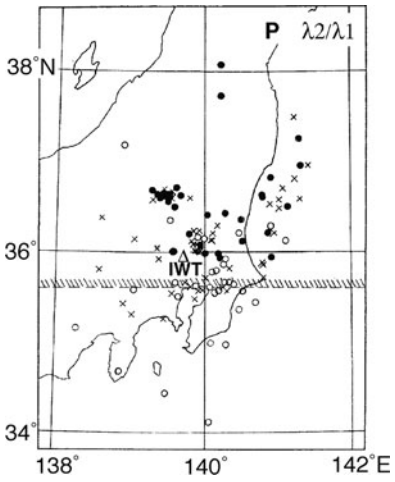

Fig. 2.34 Aspect ratio of P-wave particle motion for earthquakes in Kanto, Japan recorded at a deep borehole seismic station IWT of NRCDP (NIED). The aspect ratio is plotted at each epicenter by using open circles (0.0–0.48), crosses (0.48–0.69) and closed circles (0.69–1.0). (Matsumura 1981, Reprinted with a permission by the author and the Center for Academic Publications Japan)

in the scattering strength for S-waves. Nishizawa et al. (1983) examined the particle motion of 10 kHz-band P-wave seismograms of microearthquakes induced by water injection at the Fenton Hill geothermal site in New Mexico. They found stronger scattering for waves which traverse through the known location of a fracture zone.

The excitation of the transverse-component of motion in teleseismic P-waves was used as a measure of lithospheric heterogeneity. Nishimura et al. (2002) analyzed the energy partition of teleseismic P-wave and P-coda into the transverse-component to evaluate the lithospheric heterogeneity in the western Pacific region. They showed the presence of strong heterogeneity in and around the tectonically active regions. Kubanza et al. (2006) systematically characterized the medium heterogeneity of the lithosphere by analyzing the partition of P-wave energy into the transverse-component for $0.5 \sim 4$ Hz. Figure 2.35a shows stacked MS envelopes of teleseismic P- and P-coda waves as an example. They found significant regional differences as shown in Fig. 2.35b. The energy partition to the transverse component is small at stations on stable continents while the partition is large at stations in tectonically active regions such as island arcs or collision zones.

In Chap. 9, an extension of the Markov approximation to vector wave envelopes in random elastic media is presented to model the excitation in the orthogonal component of motion.

2.5.5 Scattering of Ultrasonic Waves in Rock Samples

In a laboratory, rock experiment by using ultrasonic waves is informative as physical simulation of wave propagation in complex media. Nishizawa and Fukushima (2008) measured ultrasonic waves on a rectangular rock prism by using a laser Doppler vibrometer, where P-waves are excited by a piezoelectric transducer (PZT)

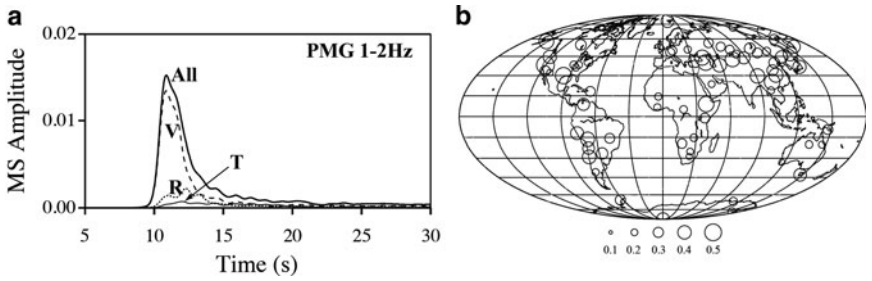

Fig. 2.35 (**a**) Stacked MS envelopes of teleseismic P-waves recorded at PMG, New Guinea in the 1–2 Hz band: V, R, T, and All for vertical-, radial-, transverse-components, and for the total, respectively. (Kubanza et al. 2007, copyright by Willey) (**b**) Spatial variation of the relative partition of transverse-component energy to the total energy in teleseismic P-waves in the 1–2 Hz band. Circles with larger radius show larger partition of energy into the transverse-component caused by scattering due to lithospheric inhomogeneity. (Kubanza et al. 2006, copyright by Terrapub)

placed on the opposite side of the rock prism as schematically illustrated in Fig. 2.36a. Figures 2.36b–d clearly show that the energy transfer from direct waves to coda waves is correlated with the scattering characteristics that depend on the grain sizes of rock media. A 0.5 MHz pulse in a medium with a P-wave velocity of 5 km/s corresponds to a 10 mm wavelength, which is closer to the grain size for the Inada granite than that for the fine-grained Westerly granite. After the arrival of the transmitted P-wave at location 'O' on the side of the sample opposite that of the source, the wave spreads in a concentric manner from that point as shown in the right column. Scattering is recognized by loss of coherence of the concentric waveform. Loss of coherence, e. g. wavefield collapsing, is the most pronounced in the Inada granite, followed by the Oshima granite and then the Westerly granite that shows a pronounced concentric circle pattern. The loss of coherence is clearly associated with the correlation length of the random heterogeneity a. The randomness of each rock sample is well characterized by the ACF. Comparison of Fig. 2.10 with Fig. 2.36 shows that the sample with the longer correlation distance has the less coherent wave-front.

Another laboratory experiment shows how the medium heterogeneity affects S-wave envelope. Figure 2.37 shows filtered three-component velocity waveforms at a distance of 80 mm from a shear PZT point source, where the mean propagation is in the z-direction and the polarization is in the x-direction at the source. For a steel block (ST), the amplitudes of direct shear waves clearly appear on the x-component, where a reflected phase is also seen in the latter part of the trace. For a small-grained gabbro block (GB) the wave duration is short at the 0.25 and 0.5 MHz bands but it becomes larger at 1 MHz. For a coarse-grained Oshima granite block (OS1), the wave duration is larger than that in GB for each frequency band. The wave duration is longer, the coda excitation is stronger, and the excitation in the z-component is the largest at the 1 MHz band. These experiments suggest that the wave envelope

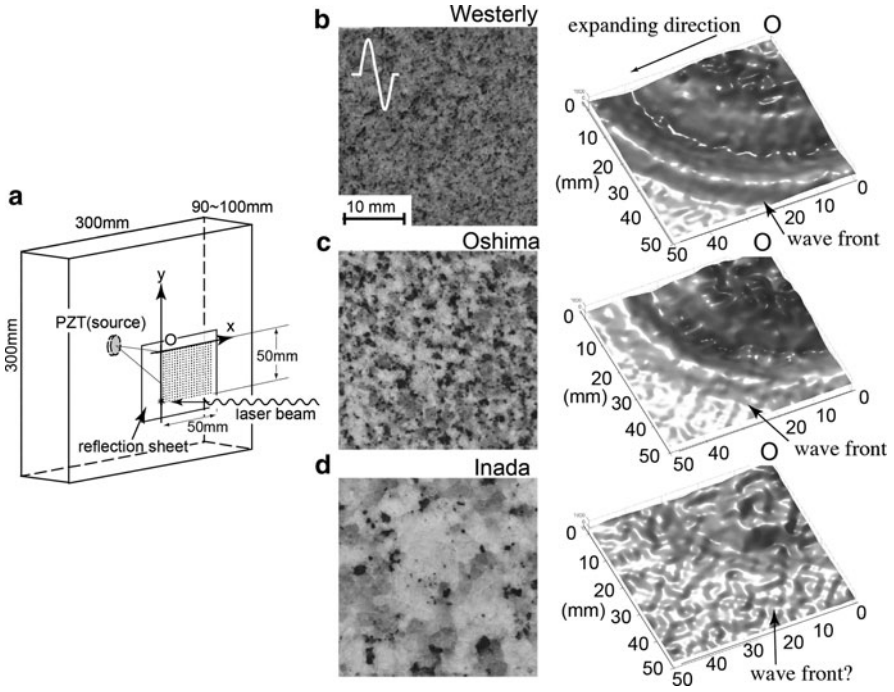

Fig. 2.36 (**a**) Measurement of wavefield on a rectangular granite rock prism excited by a PZT source. Wavefields are observed in a square area with the corner 'O' located opposite the source. Surface images of (**b**) Westerly, (**c**) Oshima, and (**d**) Inada granite samples are shown in the left column, together with snapshots of observed wavefield for the transmitted P-wave in the right column. Source signal is a 0.5 MHz sine-wave burst. The emitted wave first arrives at the corner 'O' and spreads radially outward from 'O'. The length scale and wavelength of P-wave are shown on the image of Westerly granite. (Nishizawa and Fukushima 2008, copyright by Elsevier)

duration and the excitation of the orthogonal component of motion could be good measure of medium heterogeneity.

2.5.6 Cross-Correlation Function of Ambient Noise

Since ambient noise and coda waves are a superposition of seismic waves generated and then scattered in the earth, they have a random appearance on seismograms. Campillo and Paul (2003) found that the propagation characteristics between widely separated two stations can be retrieved from the cross-correlation function (CCF) of coda waves if the time window length is long enough.

Figure 2.38 shows examples of CCFs of microseisms in the $4 - 8$ s band observed in central Japan. Microseisms of those period bands are excited in the ocean. Takagi et al. (2006) selected records of microseisms in four time periods when weather disturbances were located in differing positions surrounding Honshu,

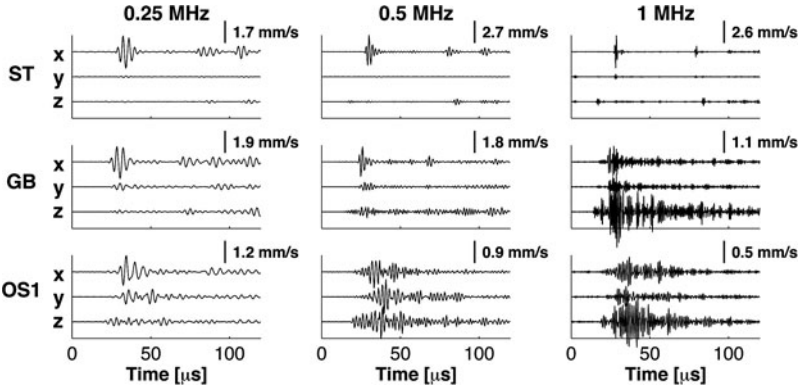

Fig. 2.37 Ultrasonic wave traces at a distance of 80 mm in the z-direction from an impulsive shear wavelet source polarized to the x-direction: ST for steel, GB for gabbro, and OS1 for Oshima granite. (Fukushima et al. 2003, copyright by the Seismological Society of America)

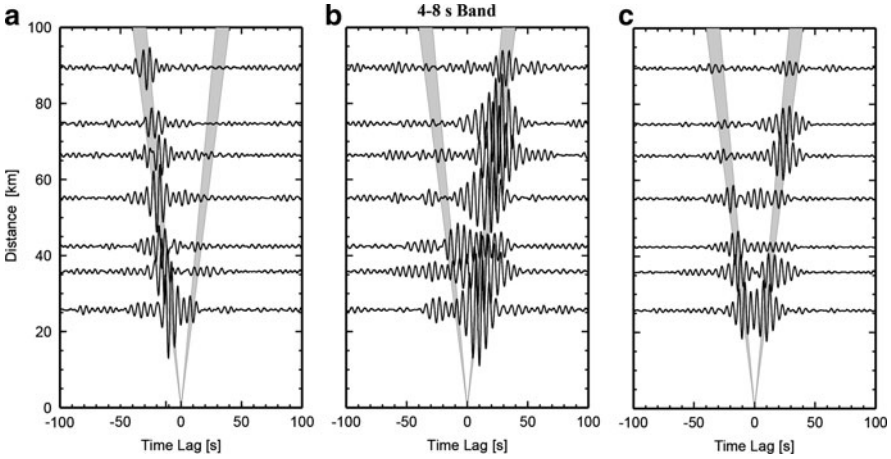

Fig. 2.38 Vertical-component CCF of microseisms registered by an array composed of Hi-net stations in Honshu, Japan: (**a**) For a period when a typhoon is in the Japan Sea (NW of the array), (**b**) for a period when a typhoon is in the Pacific Ocean (SE of the array), and (**c**) average. (Takagi et al. 2006, copyright by the Society of Exploration Geophysics of Japan)

Japan. Microseisms registered by an array composed of NIED Hi-net stations are used for the analysis, where a time window of a 36–48 h length was found to be long enough for stable measurements. For microseism CCFs, they found a good correlation between the location of the center of the typhoon and the propagation direction of microseisms. Figure 2.38a and b are microseism CCFs for a time period when a typhoon is in the Japan Sea (west of the station array) and that for a time period when a typhoon is in the Pacific Ocean (east of the station array), respectively,

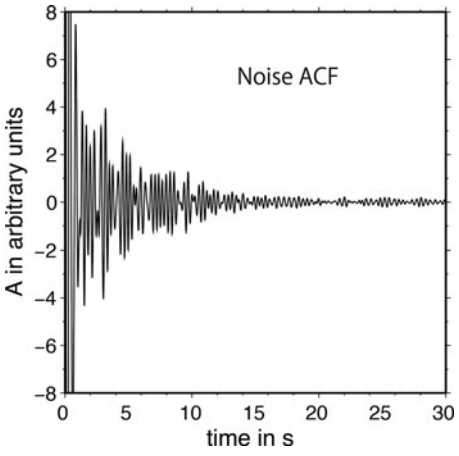

Fig. 2.39 ACF of ambient noise at station KZK of F-net (NIED) in Niigata, Japan. The 2 Hz high pass filter is applied. (Wegler and Sens-Schönfelder 2007, copyright by Willey)

where the positive time lag means westward propagation. Figure 2.38c is the average of microseism CCFs over the four periods, which is more or less symmetric with respect to lag time. These figures show clearly the propagation of Rayleigh waves with a propagation velocity of $2.7 \sim 2.8$ km/s. The CCF of ambient noise has been widely used not only for the velocity tomography of surface waves but also for that of body waves.

Wegler and Sens-Schönfelder (2007) found a similarity in the envelope amplitude decay between the tail portion of the ambient noise ACF and coda waves of a local earthquake as shown in Fig. 2.39. They noticed that the coda attenuation $Q_c^{-1} \approx 0.0066$ estimated from the coda of the ambient noise ACF at 3 Hz is in good agreement with the measurement of Q_c^{-1} from coda of local earthquakes in this region. They proposed to monitor the time shift of a coda phase of ambient noise ACF in relation with the occurrence of local earthquakes. Their study attracts interests of geophysicists to the coda portion of the CCF and ACF of ambient noise that reflects scattering characteristics of the lithospheric heterogeneities.

In Chap. 10, we will present basic mathematics for the Green's function retrieval from the CCF of random waves based on the Born scattering theory and its applications.

http://www.springer.com/978-3-642-23028-8

Seismic Wave Propagation and Scattering in the Heterogeneous Earth : Second Edition

Sato, H.; Fehler, M.C.; Maeda, T.

2012, XVI, 496 p., Hardcover
ISBN: 978-3-642-23028-8